

Guided Wave Optics Laboratory

Report No. 66

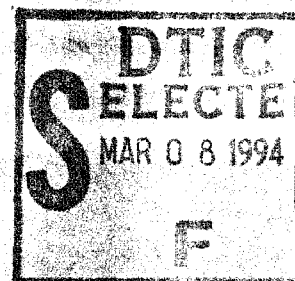
Perturbations on Effective Index
of Refraction from Prism Coupling

Stephen L. Kwiatkowski and Alan R. Mickelson

February 1995

**Department of Electrical and
Computer Engineering**

**University of Colorado at Boulder
Boulder, Colorado**



19950303 065

DTIC QUALITY INSPECTED 1



Report No. 66

**Perturbations on Effective Index
of Refraction from Prism Coupling**

Stephen L. Kwiatkowski and Alan R. Mickelson

February 1995

**Guided Wave Optics Laboratory
Department of Electrical and Computer Engineering
University of Colorado at Boulder
Boulder, Colorado 80309-0425**

Accession For	
NTIS CRA&I	<input checked="checked" type="checkbox"/>
DTIC TAB	<input type="checkbox"/>
Unannounced	<input type="checkbox"/>
Justification	
By	
Distribution/	
Availability Codes	
Dist	Avail and/or Special
A-1	

This work was supported by the National Science Foundation under Contract #ECS-9015752, the Office of Naval Research under Contract #N00014-92-J-1190, and the Army Research Office under Contract #DAAL-03-92-G-0289.

Perturbations on Effective Index of Refraction from Prism Coupling

Stephen L. Kwiatkowski and Alan R. Mickelson

Department of Electrical and Computer Engineering

University of Colorado at Boulder

Boulder, Colorado 80309

Abstract

We investigate the accuracy and precision of effective index of refraction measurements using prism coupling. The coupling gap's geometry is critical to predicting the accuracy and resolution of measurements. We provide experimental evidence that there are advantages to using high coupling pressures that yield long coupling lengths. Furthermore, effective index perturbations vary with mode number in some cases. We present and evaluate an experimental technique aimed at reducing the effects of perturbation and find that it may not be applicable to all situations. We extend a previous model of prism coupling to include a finite coupling length. This allows us to explain some of our experimental observations of m-line characteristics. We find disagreements between previous models when predicting effective index perturbations. Also, we introduce an alternative model of prism coupling based upon a local normal-mode expansion and present its preliminary numerical results. Finally, our results indicate that using prism coupling to measure effective index beyond the fourth decimal place will require additional experimental techniques and theoretical models.

Keywords: prism coupling, optical waveguide metrology, effective index.

I. PRISM COUPLING

The prism coupler couples modes of optical waveguides with the radiation modes of free space. The prism coupler can, for example, inject light into waveguides from optical sources and remove light from waveguides for detection, and is used in waveguide metrology. This paper deals with the issues of prism out-coupling as they relate to waveguide metrology, more specifically, the measurement of a mode's effective index of refraction (or, just "effective index") N .

According to [1] the first experimental results of prism-coupling light into and out of waveguides was reported in 1964 [2]. Since then, prism coupling became an area of active research with many articles describing its theory [3-11], numerical calculations of its operation [12-15], and its application to effective index measurements [16-19].

However, one aspect of prism coupling has been analyzed only for special cases and is lacking experimental investigation. This is the perturbation of the effective index by the presence of the prism. The prism locally affects the boundary conditions of the waveguide and changes the properties of effective index. This introduces an uncertainty that prevents accurate measurement of the mode effective indexes. Understanding the concept of this perturbation in prism coupling is aided by the quantum mechanical axiom which states that the act of measuring affects the outcome of the measurement.

The usual way to minimize this perturbation uncertainty is to reduce the coupling strength and therefore the coupling efficiency, to the point where m-lines are just visible enough for measurement. Theoretical investigations have been made into the conditions leading to this weak coupling but not experimental investigations. This is probably because weak coupling is often used. In fact, the weak coupling condition, to be obtained by reducing coupling pressure, is explicitly cited as part of experimental procedure for measuring N [1,17]. What is needed are experimental procedures to obtain and verify weak coupling, or better, quantify and compensate for the perturbation regardless of the coupling strength.

The need for accurate and precise measurements of effective index become especially

important when these effective indices are used to calibrate optical CAD algorithms or to design integrated optical components such as directional couplers and waveguide lenses. Calibrating waveguide fabrication parameters is one example where accurate effective index measurements are important. Usually, measuring effective indices of all the modes propagating in a waveguide is necessary to calibrate the associated fabrication process. Otherwise, overlooking some modes will result in obtaining incorrect fabrication parameters. Our experimental observations indicate that strong (not weak) coupling is needed to resolve and measure modes whose effective indices are closely spaced.

In contrast to accuracy, precision determines how exactly we measure. Measuring N within 0.01% is a typical precision requirement. For example, an uncertainty of 0.015% in effective index causes a power-coupling loss of 3 dB when designing waveguide lenses to couple light into channel waveguides.

The accuracy and precision requirements will become more strict with increasing demand for high-performance and cost-effective guided wave optical components. This is the motivation for our investigation of prism coupling. The goals of this investigation are to determine experimental procedures and theoretical models for recovering the unperturbed effective index. This includes modeling the prism-waveguide interaction, predicting the dependency of m -line characteristics such as profile and propagation direction on coupling geometry, determining the optimal set of experimental parameters, and finally, encouraging others to make additional contributions regarding perturbation effects on effective index measurements.

The organization of this paper is the following. The next section presents a first-order analysis of prism coupling. Section III follows with a discussion of previous models of prism coupling which consider perturbation effects. Section IV describes the experimental setup and the experimental procedure used throughout this paper for effective index measurements. Section V presents experimental results from investigations into perturbation effects. The final section discusses these experimental results and model predictions and compares them to other published results.

II. FIRST-ORDER ANALYSIS OF PRISM COUPLING

Figure 1 schematically illustrates the relevant features and parameters of output prism coupling. This is the prism coupling set-up used to make the effective index measurements reported throughout this paper. Pressing a prism onto the surface of a waveguide forms the prism-coupler. A requirement for successful prism coupling is that the prism's index of refraction must be greater than the waveguide mode's effective index. The coupling between the prism and waveguide mode extends over the length L_c . We estimate from experimental observations that the coupling length is several hundred micrometers. The height of the gap determines the coupling strength between the prism and waveguide. In some cases, spacers are used to engineer the gap's geometry [10]. Other times dust particles and surface irregularities determine the gap's geometry. The height of the gap should be a fraction of a wavelength to efficiently couple light from the waveguide. However, the gap should be as large as possible during effective index measurements to minimize perturbation effects. The out-coupled radiation forms irradiance patterns called m-lines. Each m-line is associated with a particular waveguide mode. Furthermore, the gap geometry and the mode's effective index determine the characteristics of each m-line.

Next, we present a first-order analysis describing the measurement of the effective index using m-lines. This analysis is for weak coupling and assumes the prism and waveguide are composed of loss-less dielectric materials. In addition, we assume a uniform gap of infinite length. Afterwards, in Section II B we discuss the m-line's irradiance distribution, or profile.

A. Analysis of the Effective Index Measurement

The following description of out-coupling a waveguide mode through a prism uses coupled-mode theory [1,20,21]. This description applies to weak coupling where the presence of the prism does not alter the mode's effective index. The waveguide mode propagates along the waveguide until it reaches the region of the prism. Here, the waveguide mode's

evanescent tail interacts with the prism's higher index of refraction. This interaction causes the waveguide modes to couple with a prism radiation mode. The radiation mode propagates in a particular direction determined by satisfying the phase-matching condition. The phase-matching condition is given by

$$N_m = n_p \sin \theta_m, \quad (1)$$

where n_p is the prism's index of refraction, and θ_m is the radiation angle internal to the prism that is determined by a particular effective index N_m .

The radiation mode continues to propagate away from the waveguide at the angle θ_m until exiting the prism. There, it refracts into the radiation angle θ'_m according to Snell's law. The optical irradiance distribution associated with this radiated mode appears as a distinct line at distances greater than about 1 m from the prism. This pattern of light is called a bright m-line or just an m-line. Measuring the m-line's radiation angle θ'_m determines the effective index according to [1]

$$N_m = n_p \sin \left[\phi_p + \arcsin \left(\frac{n_c}{n_p} \sin \theta'_m \right) \right], \quad (2)$$

where ϕ_p is the prism's angle, and $n_c = 1$ is the index of air. Furthermore, the m-line associated with each mode will radiate at a different angle because every mode has a different effective index.

B. Analysis of the M-Line's Profile

This section presents an analysis describing the m-line's profile by combining the first-order coupled-mode model with an extension of the analysis by Tien [6]. This analysis expands Tien's work to include a finite coupling length and extends his analysis to predict the m-line's far-field irradiance distribution using the radiation angle of Section II A. First, we summarize the analysis by Tien.

Tien uses the concept of optical tunneling to describe the penetration of optical power across the gap's refractive index barrier. Figure 2 shows a diagram of output prism coupling

illustrating the concepts used in Tien's analysis. A waveguide mode has initial amplitude $b_1(z = 0)$ at positions $z \leq 0$. This mode begins to interact with the prism at $z = 0$, where it couples to the radiation mode of amplitude $b_3(z)$. The coupling continues for all $z \geq 0$. This coupling depletes the field amplitude of the waveguide mode according to

$$\frac{db_1(z)}{dz} = -S b_1(z), \text{ for } 0 \leq z \leq L_c, \quad (3)$$

where S is the coupling strength. The coupling strength is constant for all $z \geq 0$. The solution to Equation (3) is

$$b_1(z) = \begin{cases} b_1(0) & \text{for } z < 0 \\ b_1(0) \exp(-S z) & \text{for } z \geq 0 \end{cases} \quad (4)$$

The power lost by the waveguide mode at any position $z \geq 0$ is proportional to $b_1(z) b_1^*(z)$. This power reappears in the prism as the radiation mode b_3 . Consequently, the z -dependence of the radiation mode's field amplitude is

$$b_3(z) = \begin{cases} 0 & \text{for } z < 0, \\ b_3(0) \exp(-S z) & \text{for } z \geq 0. \end{cases} \quad (5)$$

Equation (5) is the relevant result of Tien's analysis. This result shows that the initial field distribution of radiation mode (or m-line) is a decaying exponential along the z -axis.

We can extend Tien's result by combining the field distribution in Equation (5) with a propagation direction. This will allow us to calculate the m-line's far-field irradiance distribution. The m-line's propagation direction was given by the phase-matching condition in Equation (1). Furthermore, we can truncate the initial field distribution by introducing a finite coupling length L_c . Thus, using the phase-matching angle and the finite coupling length, we write the m-line's complete initial field distribution (omitting the harmonic time dependence) as

$$b_3(x, z) = \begin{cases} 0 & \text{for } z < 0, \\ b_3(0) \exp(-S z) \exp[in_p k(x \cos \theta_m + z \sin \theta_m)] & \text{for } 0 \leq z \leq L_c, \\ 0 & \text{for } z > L_c, \end{cases} \quad (6)$$

where $k = 2\pi/\lambda$ and λ is the wavelength of free space. In addition, we express $b_3(z)$ in a rotated coordinate system (x_r, z_r) such that the m-line's propagation direction is along x_r :

$$b_3(x_r, z_r) = \begin{cases} 0 & \text{for } z_r < 0, \\ b_3(0) \exp(i n_p k x_r - S z_r \sec \theta_m) & \text{for } 0 \leq z_r \leq L_c \cos \theta_m, \\ 0 & \text{for } z > L_c \cos \theta_m. \end{cases} \quad (7)$$

Equation (7) describes the m-line's initial field distribution, which we will propagate into the far field. Figure 3 sketches the form of $b_3(x_r, z_r)$ illustrating the rotated coordinates x_r and z_r . The field distribution in Equation (7) is similar to the result of the analysis based on leaky modes found on pages 102-103 of [1]. Those results differ from Equation (7) by omitting the effects of a finite coupling length. Next, we calculate the m-line's far-field irradiance distribution.

Consider Equation (7) as describing the field in a coordinate system z_r . We define a new coordinate system z'_r which is a distance x_r from z_r . We would like to find the field distribution b'_3 in the z'_r coordinate system. We will ignore prism boundaries and assume the m-line propagates in a half-space of refractive index n_p . If x_r satisfies the Fraunhofer, or far-field, requirements [22] then b'_3 is found using

$$b'_3(x_r, \nu) \propto \int_{-\infty}^{\infty} b_3(x_r, z_r) \exp(i 2\pi n_p \nu z_r) dz_r, \quad (8)$$

where

$$\nu \equiv \frac{z'_r}{\lambda x_r}. \quad (9)$$

Substituting Equation (7) into Equation (8) yields

$$b'_3(x_r, \nu) \propto \int_0^{L_c \cos \theta_m} \exp[(i 2\pi n_p \nu - S \sec \theta_m) z_r] dz_r \exp(i n_p k x_r). \quad (10)$$

Evaluating the integral in Equation (10) yields

$$\begin{aligned} b'_3(x_r, \nu) &\propto \frac{\exp[(i 2\pi n_p \nu - S \sec \theta_m) z_r]}{i 2\pi n_p \nu - S \sec \theta_m} \Big|_0^{L_c \cos \theta_m} \exp(i n_p k x_r) \\ &\propto \frac{\exp[(i 2\pi n_p \cos \theta_m \nu - S) L_c] - 1}{i 2\pi n_p \nu - S} \exp(i n_p k x_r). \end{aligned} \quad (11)$$

The far-field irradiance distribution I'_3 is proportional to $(b'_3)(b'_3)^*$ yielding

$$I'_3(x_r, \nu) \propto \frac{1 + \exp(-S L_c) [\exp(-S L_c) - 2 \cos(2\pi n_p \cos\theta_m \nu L_c)]}{S^2 + (2\pi n_p \nu)^2} \quad (12)$$

$I'_3(x_r, \nu)$ depends on z'_r by way of $\nu \equiv z'_r/\lambda x_r$.

Equation (12) predicts the far-field characteristics of the m-line's irradiance distribution within the frame work of the first-order analysis for weak coupling and uniform gap height. One other simplifying approximation was the omission of the prism boundary. Thus, Equation (12) neglects the refraction of the m-line at the prism-air interface. One straightforward way to include refraction that remains within the confines of the first-order model assumes that the m-line has a planar phase front when it reaches the index boundary. Then we can apply Snell's law and use another appropriately rotated coordinate system in which to express the far-field distribution. This planar phase-front assumption is implied in the development of Equation (2).

A higher-order correction for refraction at the prism boundary can be made to Equation (12). For example, we could regard the index boundary as being in the near-field or Fresnel zone of the initial field distribution. Thus, we would propagate the field b_3 in Equation (7) to the index boundary using Fresnel approximations [22]. There, we could incorporate Snell's law and finish the propagation to the far field.

Even without making this modification we can still use Equation (12) qualitatively to identify certain m-line characteristics that will aid in effective index measurements. Equation (12) predicts a maximum value for I'_3 at $z'_r = 0$. This means that the irradiance maximum propagates at the radiation angle θ'_m . We can use this m-line characteristic to measure the radiation angle θ'_m and thus determine N_m . We can accomplish this by first determining the radiation angle from a geometric construction that is formed by tracking the position of the irradiance maximum for two different values of x_R . Then, we can calculate N_m using Equation (2).

Another m-line characteristic given by Equation (12) is the dependence of the irradiance distribution on coupling length L_c . For a given weak coupling strength (small S) the irra-

diance distribution will be broader for short L_c , and conversely, narrower for long L_c . This characteristic will have consequences regarding the resolving power of the prism coupler.

One consequence of coupled-mode theory is that energy couples from the first mode to the second, and then back to the first mode. Even though this back-and-forth coupling results from the mathematics, there is neither the experimental evidence nor any aspect of the physical model for prism coupling to support this result. One possible way to resolve this point is to consider that the necessary coupling length for the return coupling is longer than L_c .

While this first-order model does not predict perturbations on the effective index, it provides a qualitative description of the m-line's far-field irradiance distribution. The next Section discusses higher-order models which calculate the effective index perturbation for the weak coupling.

III. PREVIOUS MODELS OF PERTURBATION EFFECTS

The first-order model of the last does not determine the perturbation to the effective index due to the prism. Previous models address effective index perturbations, but they do so in the context of input prism coupling. The approaches taken by these previous models include transverse resonance [1], ray optics [11], a combination of ray and wave optics [3], optical tunneling [6], plane-wave expansion [4,5], and the matrix method [12-15].

Ulrich [4] provides numerical results and analytical expressions for the perturbation of effective index. For strong coupling, Ulrich plots numerical results (in his Figure 3) showing that the effective index of all the waveguide modes decreases as the gap height decreases (coupling strength increases). Others [11,12,14] report the same relationship between effective index and coupling strength in the strong coupling regime. While another group [15] reports the opposite relationship between increasing effective index and coupling strength. In [15] numerical calculations show that effective index increases with increasing coupling strength over both weak- and strong-coupling regimes.

Ulrich's analytical results for weak coupling predicts that δN can vary in magnitude and sign for each waveguide mode, and the existence of a particular prism refractive index which yields $\delta N = 0$ for a particular effective index. Unfortunately, we must know the unperturbed mode indices in addition to the gap height in order to calculate the perturbation when using Ulrich's analysis. This requirement prohibits using Ulrich's analysis to recover unperturbed effective indices from their measured values unless the perturbation is assumed to be so small that the measured effective index could be used in the calculation.

Next, we apply Ulrich's analytical expressions to another case reporting numerical results for effective index perturbations. This case is from Walpita [14], who reports effective index decreasing as coupling strength increases. His plot of effective index versus gap height (his Figure 10) clearly shows that the effective index decreases with increasing coupling strength. The range of gap heights in his Figure 10 spans from strong coupling to weak coupling. However, we find the opposite relationship between gap height and effective index for this prism-waveguide structure and range of gap heights using Ulrich's analytical expressions.

IV. EFFECTIVE INDEX MEASUREMENT

In this section we show how we measure effective index and why we use this method.

We base our measurement on the concepts and relationships in the first-order model of Section II. Our method includes a procedure to yield relative rather than absolute effective index. We resort to measuring the effective index relative to the substrate index in order to reduce the influence of the prism perturbation and other residual systematic uncertainties. This procedure uses an m-line which is associated with a substrate radiation mode. The advantage of using this procedure is that we do not require a model to predict prism perturbation effects, nor do we need to determine the gap's geometry. However, a disadvantage of reporting relative effective index is that the measurement uncertainty increases due to adding the uncertainty in measuring the mode's m-line to the uncertainty in measuring the substrate's m-line.

The following section describes our experimental setup for measuring the effective index. Section IV B describes the relative measurement procedure and is followed by Section IV C describing uncertainty analysis.

A. Experimental Setup

Figure 4 illustrates the experimental setup we use to measure effective index. Laser light at wavelengths $\lambda = 0.6328 \mu\text{m}$ or $\lambda = 0.829 \mu\text{m}$ is butt-coupled into the slab waveguide using a single-mode polarization-maintaining fiber. The extinction ratio between the two orthogonally polarized modes of the fiber was greater than 400:1. A rutile prism with its optic axis parallel to the waveguide's optic axis is pressed against the waveguide to couple light out from the waveguide. The prism's index of refraction at our operating wavelengths can be found in Table I. At the output face of the prism, the m-line is refracted into air (index of refraction of air is $n_c = 1.0003$) at the radiation angle θ'_m . The relationship between a mode's effective index N_m and θ'_m is given by Equation (2).

In order to measure θ'_m , we aligned two translation stages, one with travel parallel to the prism output face and one with travel perpendicular to the prism output face. A windowless charge-coupled device (CCD array) is affixed to these stages at a distance of approximately 1 m from the prism output face. The m-line illuminates the CCD array, and a profile of the m-line is viewed on a digital oscilloscope while a TV monitor displays the entire CCD field. We measure the m-line's radiation angle $\theta'_{m,s}$ in the translation stages' coordinate system (x_s, y_s) using triangulation. A right triangle is formed by translating the CCD array a distance Δy_s and a perpendicular distance Δx_s . For a particular translation $\Delta y_s = 50.00$ mm, the translation Δx_s is determined by repositioning the m-line at the location on the CCD array. Now, we can calculate the mode angle using the equation

$$\tan \theta'_{m,s} = \frac{x_s}{y_s} . \quad (13)$$

Note however, that Equation (2) requires we know the m-line's radiation angle θ'_m in the prism coordinate system (x_p, y_p) . Thus, we must determine the alignment between the

prism's coordinate system and the stages coordinates system. We determine this alignment using a dial indicator gauge mounted on the translation stage assembly. We position its indicator tip to be under pressure contact with the prism's output face (see Figure 5). The dial registers the displacement along y_s necessary to maintain contact between the tip and the prism's output face as the dial indicator translates along x_s . Recording the translations Δx_s and Δy_s allow us to calculate the rotation angle γ between the two coordinate systems using

$$\gamma = \arctan \left(\frac{\Delta y_s}{\Delta x_s} \right). \quad (14)$$

Once γ is known then the radiation angle in the prism's coordinate system can be found using

$$\theta'_m = \theta'_{m,s} - \gamma. \quad (15)$$

The inset of Figure 5 illustrates these angular relationships (all of the angles for this particular case are negative).

The measurement of θ'_m has several sources of systematic uncertainty which affect the calculation of N_m . These sources include the uncertainty in both the prism angle and the prism index, the uncertainty of both the alignment and travel of the stages, and the perturbation due to waveguide-prism coupling. The next section describes our procedure which reduces the influence of these sources of uncertainty.

B. Relative Effective Index Measurements

The procedure for making relative effective index measurements uses the substrate radiation mode. The substrate radiation mode propagates with a value of effective index N_{sub} that lies between 0 and the substrate index of refraction n_{sub} :

$$0 \leq N_{sub} \leq n_{sub}. \quad (16)$$

This substrate radiation mode is excited by positioning the input fiber a distance d perpendicular to the plane of the waveguide; see Figure 6. As $d \rightarrow 0$, the value of θ'_m for the radiation mode approaches the value of the substrate angle θ'_{sub} . This follows from the phase-matching condition [Equation (1)] illustrated in the inset of Figure 6. The substrate m-line distinguishes itself from the m-lines of guided modes as its position moves on the CCD array as the input fiber position changes (d changes). In addition to moving with d , the maximum irradiance of the substrate m-line decreases as $d \rightarrow 0$. Thus, we equate $\theta'_m \equiv \theta'_{sub}$ when d is near 0 and the irradiance of the substrate m-line is still far enough above the noise to make a confident measurement of the radiation angle.

The substrate index N_{sub} is calculated from θ'_{sub} using Equation (2). A value of N_{sub} is obtained for each effective index measurement and is subtracted from the value of N_m for the guided mode. This relative value $\Delta N_m = N_m - N_{sub}$ yields the increment by which the effective index exceeds the substrate index. We reduce the influence of systematic uncertainties, including the influence of the prism's perturbation effects, by taking this difference and assuming that the prism's perturbation is the same for both the guided modes and the substrate mode.

C. Measurement Uncertainty Analysis

Uncertainty with the measured values of ΔN_m due to the random uncertainty of repositioning the m-line on the CCD array remains. The uncertainty bars displayed in the plots of ΔN presented throughout this paper represent this measurement uncertainty. We determine this component of the measurement uncertainty as follows. First, we determine the uncertainty of measuring the radiation angle θ' using the differential of Equation (13)

$$\begin{aligned} d\theta'_m &= \left| \frac{\partial \theta'_m}{\partial x_s} dx_s - \frac{\partial \theta'_m}{\partial y_s} dy_s \right| \\ &= \left| \frac{\frac{1}{y_s} dx_s - \frac{x_s}{y_s^2} dy_s}{1 + \left(\frac{x_s}{y_s}\right)^2} \right|. \end{aligned} \quad (17)$$

Typical values of the parameters in Equation (17) for the waveguide mode under study here are $y_s = 50.00 \pm 0.01$ mm and $x_s \approx y_s/2 \pm 0.01$ mm. Our experimental apparatus limits the measurement uncertainty dy_s while m-line characteristics determine the measurement uncertainty dx_s as we reposition the m-line on the CCD array. These experimental measurement uncertainties yield a maximum uncertainty in the radiation angle

$$\begin{aligned} d\theta'_m &= 2 \times 10^{-4} \text{ rad} \\ &= 0.01^\circ \end{aligned} \quad (18)$$

when using opposite signs for dx_s and dy_s . There are instances when the m-line characteristic allows the uncertainty in x_s to be as small as ± 0.005 mm or as large as ± 0.03 mm. Thus, each measurement carries along its own uncertainty.

Next, we determine the uncertainty in ΔN_m to be

$$d\Delta N_m = \frac{\partial N_m}{\partial \theta'_m} d\theta'_m + \frac{\partial N_{sub}}{\partial \theta'_{sub}} d\theta'_{sub} \quad (19)$$

using the differential once again. We use a plus sign in Equation (19) so that we calculate the largest uncertainty in $d\Delta N_m$. Values of the partial differentials in Equation (19) lie between 0.008 and 0.01 using typical parameters for the our waveguides at both wavelengths. Taking the larger value and using Equation (18) yields the measurement uncertainty

$$d\Delta N_m = \pm 2 \times 10^{-4} \quad (20)$$

The next section presents some example m-line irradiance profiles and a case history for a particular set of effective index measurements. This case history includes using the effective index measurements to determine waveguide fabrication parameters and comparing these parameters to analytical measurements.

D. Example M-Line Profiles and Effective Index Case History

M-line irradiance profiles at $\lambda = 0.6328 \mu\text{m}$ for the fundamental mode of a titanium in-diffused planar waveguide are shown in Figure 7. These two profiles correspond to the

two propagation distances forming the right triangle in the geometric construction for determining the m-line radiation angle. The far propagation distance is 1.24 m and the difference between propagation distances is 50.00 mm. The m-line profile propagating furthest is slightly wider, as expected. However, we find different divergence angles for these profiles using

$$\theta_d = \arctan\left(\frac{\text{FWHM}}{2D}\right), \quad (21)$$

where D is the propagation distance. We calculate $\theta_d = 0.522 \pm 0.005$ mrad for the near profile while $\theta_d = 0.549 \pm 0.005$ mrad for the far profile. The divergence angles should be the same if these profiles are in the far-field of the m-line's source (the prism-waveguide gap). Also notice the slight asymmetry in these irradiance profiles. The profiles from a uniform gap should be symmetric according to the first-order model in Section II B (Equation (12)). This asymmetry and the unequal divergence angles could indicate that these profiles are not in the far-field of the gap.

We investigate the effects of propagating only into the Fresnel zone on our measurement. We use coupling length $L_c = 1$ mm, coupling strength $S_c = 0.00035 \mu\text{m}^{-1}$ and $\lambda = 0.6328 \mu\text{m}$ to calculate the m-line's irradiance profile using the Fresnel propagating equations. We find that the maximum irradiance does not occur at $z_r = 0$ but is offset along $+z_r$. We plot this perpendicular displacement from the far-field propagation direction versus propagation distance in Figure 8. We see that the displacement become nearly constant after propagating 30 cm. Thus, the position of the m-line's maximum irradiance follows a path nearly parallel to the x_r axis. We calculate an additional uncertainty of $\pm 1 \times 10^{-6}$ in ΔN using our method after a propagation distance of only 30 cm. We consider this uncertainty negligible since it is two orders of magnitude less than the uncertainty already accounted for in the previous section.

Next, we use the methods outlined in the previous section to measure effective index in a set of titanium in-diffused, lithium niobate slab waveguides. The waveguides are formed on y-cut wafers, and the waveguide modes propagate parallel to the crystal's x-axis. The input

light is polarized along the crystal's y-axis to excite TM-polarized guided modes. These modes will guide because of the increase in lithium niobate's ordinary index of refraction due to titanium in-diffusion [23]. The TM-polarization was chosen over TE-polarization to avoid confusion arising from other coincident diffusion processes affecting lithium niobate's extraordinary index of refraction [24,25].

The diffusion time t , the titanium thickness τ , the diffusion coefficient $D(T)$, and the diffusion temperature T are the parameters for titanium concentration $C(y, t; D(T), \tau)$ after diffusion [26]. Converting titanium concentration to a change of index of refraction $\Delta n(y, t)$ introduces two more parameters [27]. These are η and K , where

$$\Delta n(y, t) = (K C(y, t; D(T), \tau))^\eta. \quad (22)$$

We would like to determine $D(T)$, η , and K . We accomplish this by fabricating four waveguide specimens using the same parameters except for diffusion time. The common parameters are $T = 1000^\circ\text{C}$ and $\tau = 25$ nm. The diffusion times are $t = 1, 2, 4, 8$ h. Then we measure the effective index ΔN of the modes in these waveguides. Finally, we compare these measured mode effective indices to those calculated using the index profile given by Equation (22). This comparison is shown in Figure 9, where we plot effective index versus diffusion time. The parameter values used to fit the theoretical curves to the measured data are

$$\begin{aligned} K &= 0.033, \\ \eta &= 0.62, \\ D &= 0.2 \mu\text{m}^2/\text{h}. \end{aligned} \quad (23)$$

There is good agreement between the measurements and fitted curves for both effective index and number of guided modes.

We use D in Equation (23) to calculate the titanium concentration profile for diffusion time $t = 2$ h using the Gaussian solution to the diffusion equation [26]. Then we compare this calculated profile to that which was measured in specimen 42 (2 h diffusion) using

secondary ion mass spectroscopy (SIMS). Figure 10 shows this comparison. We find better agreement between the calculated and measured titanium concentration profiles using $D = 0.245 \mu\text{m}^2/\text{h}$.

V. EFFECTIVE INDEX PERTURBATIONS

The previous sections illustrate the theoretical impact of the prism-waveguide perturbation on effective index measurements. In this section we discuss our experimental observations regarding measurement perturbations starting with coupling gap geometry.

A. Coupling Gap Geometry

We have pointed out the importance of the gap height s and the coupling length L_c on effective index measurements. Our experimental observations indicate the gap is nonuniform over the contact region, contrary to the illustration in Figure 1. In fact, Newton's rings are visible when the gap is viewed through the waveguide's substrate. These nearly concentric interference fringes delineate regions of equal gap height. Both the spacing and distribution of these fringes change as the pressure changes. To see this, consider the prism as a rigid body while the waveguide is an elastic body undergoing pure bending without compression or extension. Figure 11 illustrates the initial contact between waveguide and prism for low coupling pressure. Here, the planar waveguide contacts the prism at three points determined by surface inhomogeneities. At this pressure there is a minimum gap height s_{\min} and a coupling length L_c (actually the coupling occurs over an area) over which the gap height is less than some critical height. The critical gap height s_c is defined to be the height at which the interaction between prism and waveguide becomes insignificant. Nearly parallel and equally spaced interference fringes are seen at this initial contact. Increasing the coupling pressure causes the waveguide to bend (Figure 11). For example, this can decrease the minimum gap height to s'_{\min} and also move its positions and that of s_c . Thus, higher pressure can result in both a different coupling strength and a different coupling length.

The coupling length increases in this case. The interference fringes become more concentric and unevenly spaced at higher pressures. Later, we will show how these effects can change the characteristics of m-lines and therefore, affect the measurement of N .

We cannot associate a stronger coupling pressure with a smaller gap height or a longer coupling length since we are unable to accurately quantify the gap's geometry. In fact, we cannot rule out that s could be unchanged by increasing the coupling pressure.

Next, we present experimental results regarding the perturbation effects on both the m-line's radiation angle and its irradiance profile.

B. M-Line's Radiation Angle and Profile Perturbations

We report two data sets (Set 1 and Set 2) measuring the variation of effective index with applied coupling pressure on waveguide specimen 56. Waveguide specimen 56 is a titanium in-diffused, lithium niobate slab waveguide. The fabrication parameters for specimen 56 are, 25 nm of titanium evaporated on y-cut lithium niobate, and a 2 h diffusion at 1000°C in flowing argon. The waveguide modes propagate parallel to the crystal's x-axis. The input light is polarized along the crystal's z-axis (TE-polarized). We cannot compare coupling pressures between the data sets because the specimen was removed and then remounted for each data set. Furthermore, we do not use the substrate m-line in these measurements because we want see the influence of the perturbation. Thus, we report absolute effective index here.

Table II shows Set 1 effective index measurements at $\lambda = 0.6328 \mu\text{m}$ for two different coupling pressures $P_1^{(1)}$ and $P_2^{(1)}$, where $P_1^{(1)} < P_2^{(1)}$ (the parenthetic superscript 1 denotes Set 1). The fundamental mode TE-0 shows an effective index decrease of 0.0022 as the coupling pressure increases. However, the effective index of the lowest order mode TE-3 shows an increase of 0.0005 with the same increase in coupling pressure.

Figure 12 compares the m-line irradiance profiles of the TE-0 mode at coupling pressures $P_1^{(1)}$, $P_2^{(1)}$. We see that the m-line profile's full width at half maximum FWHM decreases as

the coupling pressure increases. Likewise, Figure 13 compares the TE-3 mode m-line profiles at these two pressures. A similar decrease of FWHM with increasing coupling pressure is seen in the TE-3 mode m-line. Also Figure 13, there is poor separation between the TE-2 and TE-3 modes at pressure $P_1^{(1)}$, while the resolution between these modes improves at the higher pressure $P_2^{(1)}$. Furthermore, the m-line profiles at the higher pressure $P_2^{(1)}$ are nearly symmetric while the profiles at the lower pressure $P_1^{(1)}$ are asymmetric.

We make further comparisons between the m-line profiles in Figures 14 and 15. Figure 14 compares the TE-0 and TE-3 m-line profiles at low coupling pressure $P_1^{(1)}$ while Figure 15 makes the same comparison but at high coupling pressure $P_2^{(1)}$. The m-line profiles of the two modes have similar shapes at each coupling pressure. Furthermore, the FWHM of modes TE-0 and TE-3 are nearly identical at $P_1^{(1)}$ while the FWHM of TE-0 is larger than the FWHM of TE-3 at $P_2^{(1)}$.

In each of the Figures 12 through 15 we normalized the maximum irradiance to 1 and shifted the profiles so that the maximum is at far-field angle $\theta_f = 0$. The far-field angle is calculated using

$$\theta_f \equiv \frac{z'_r}{x_r}, \quad (24)$$

where z'_r is the position along the CCD array and $x_r = 1.17 \pm 0.02$ m is the propagation distance.

Table III shows Set 2 of effective index measurements at $\lambda = 0.6328 \mu\text{m}$ for three different coupling pressures $P_1^{(2)}$, $P_2^{(2)}$ and $P_6^{(2)}$ where $P_1^{(2)} < P_2^{(2)} < P_6^{(2)}$. The changes in effective index are smaller here in Set 2 than they are in Set 1. In fact, most of the changes here are within the measurement uncertainty. An important observation from Table III is the appearance of mode TE-4 at coupling pressures $P_2^{(2)}$ and $P_6^{(2)}$. This mode was not seen in Set 1 nor at coupling pressure $P_1^{(2)}$.

The FWHM of various modes at coupling pressures $P_1^{(2)}$ through $P_7^{(2)}$ are shown in Figure 16. The coupling pressure increases from $P_1^{(2)}$ to $P_7^{(2)}$. The FWHM of mode TE-0 increases with each increase in coupling pressure. The FWHM of mode TE-4 also increases

from pressure $P_6^{(2)}$ to $P_7^{(2)}$. In contrast, the FWHM's of modes TE-1 and TE-2 decrease with increasing coupling pressure. In comparison, the difference in FWHM between modes TE-0 and TE-3 of Set 1 is 0.5 in the same units as Figure 16.

In the next section we present results of measuring the substrate effective index in the presence of the prism perturbation.

C. Perturbation of the Substrate's Effective index

We use the substrate's effective index in our effective index measurements (Section IV) to remove the effects of the prism perturbation. In this section we report how the substrate effective index deviates from the predictions of the phase-matching condition for the unperturbed interaction.

The substrate effective index (Section IV B) should vary sinusoidally with angle of incidence according to the phase-matching condition, Equation (1) and Figure 6. Two measurement sets were made of N_{sub} versus angle of incidence θ_i at $\lambda = 0.829 \mu\text{m}$. First Set A was measured and then Set B. Figure 17 illustrates these data sets. Each plot symbol in Figure 17 represents at least 3 repeated measurements. The measurements of Set A yields wide variations in N_{sub} at angle of incidences between 87.5° and 90° . While the variation in N_{sub} of Set B are smaller. Comparing the measurements of these two data sets at $\theta_i = 89.5^\circ$ yields the result that the Set B measurement of N_{sub} is greater than the Set A measurement of N_{sub} . However, the opposite relationship is found at $\theta_i = 89.5^\circ$. Furthermore, the measurements of Set B and Set A nearly coincide at $\theta_i = 89.8^\circ$ and at $\theta_i = 85.5^\circ$. We cannot explain these inconsistencies.

We are able to measure the substrate effective index at angles up to $\theta_i = 89.76^\circ$ where the substrate m-line begins to interfere with the m-line from the highest order guided mode. The Set B measurement at this angle of incidence yields $N_{sub} = 2.1721$. The square plot symbol in Figure 17 represents the measurement of the highest order guided mode's effective index $N = 2.1726$. We subtract this substrate's effective index from the guided mode's effective

index to yield the relative effective index ΔN described in Section IV B.

The solid curve in Figure 17 represents calculations of substrate effective index fit to the measurements for $\theta_i \leq 87.5^\circ$ using the phase-matching condition. The substrate index $n_{sub,f}$ is the fitting parameter and has value $n_{sub,f} = 2.1712$.

VI. DISCUSSION

We have attempted to reduce perturbation effects on effective index measurements by recording relative rather than absolute measurements. This technique assumes that the perturbation is the same for all waveguide modes. However, our observations of effective index perturbation include cases where the effective index perturbation varies measurably with each waveguide mode (Table II) and cases where it does not (Table III). We attribute this variability in effective index perturbations to the geometrical details of the coupling gap. Consequently, our relative measurements aimed at reducing the perturbation effects on effective index may not be applicable to all cases. Unfortunately, we know of no other experimental techniques which can reduce the effective index perturbations without also sacrificing resolution.

In addition to affecting the m-line's radiation angle, the gap geometry also affects the m-line's irradiance profile. Figures 12 and 13 illustrate that m-lines can narrow with increasing coupling pressure. This narrowing provides better resolution for closely spaced m-lines. In fact, we have also seen what at first appears to be one m-line split into two m-lines representing two very closely spaced modes as the coupling pressure increases. Thus, we see advantages to using high coupling pressures. This is at odds with the recommendations that effective index measurements should only be made at low coupling pressures to avoid perturbations [1,12]. However, if we use high coupling pressures, then we must be prepared to recover the unperturbed effective index. Otherwise, we are not taking full advantage of the additional resolution and we are just trading resolution enhancements for a reduction in measurement precision.

We also present evidence in Figure 16 that m-lines broaden with increasing coupling pressure. We can reconcile these observations with those in Figures 12 and 13 if we do not always correlate coupling pressure with coupling strength. For example, we can imagine in one case that increasing the coupling pressure causes a longer coupling length while the coupling strength remains constant (or, equivalently gap height remains constant), whereas in another case, increasing the coupling pressure increases the coupling strength while leaving the coupling length unchanged. Using the first-order model, we find in the first case that the m-line profiles narrow with increasing coupling pressure if the product $S_c L_c \approx 1$ but remains unchanged if $S_c L_c \gg 1$. In contrast, the second case will result in the m-line's profile broadening as coupling pressure increases. This was probably the situation when others observed m-line broadening with increasing coupling strength [16,17].

Our measurements of substrate effective index produce more interesting results. For example, the measurements of N_{sub} at angle $\theta_i \leq 87.5^\circ$ in Figure 17 can be fitted to the unperturbed phase-matching condition using a substrate index of refraction $n_{sub,f} = 2.1712$. We are not surprised to find that $n_{sub,f}$ differs from the unperturbed substrate index of refraction $n_{sub} = 2.1728$ [28]. However, we find it interesting that the measurements of N_{sub} at angle of incidences $\theta_i \geq 87.5^\circ$ yield values that deviate from the fitted curve and approach the unperturbed index of refraction. The fiber displacement is $d = 10 \mu\text{m}$ (see Figure 6) at the largest angle of incidence ($\theta_i = 89.76^\circ$) that we can measure N_{sub} . This places the fiber's input coupling point within the substrate, below the region of titanium in-diffusion. Thus, light from the fiber should propagate with the substrate's index of refraction even at this extreme angle of incidence.

Our observations of m-line characteristics show that there are two important parameters of the coupling gap. These are the gap height, which determines how significant are the effective index perturbations, and the coupling length, which influences inter-modal resolution. The coupling pressure does not always correlate with either of these gap characteristics in a consistent manner, probably due to the details surrounding the formation of the gap. Furthermore, waveguide material properties could be as important to gap geometry as cou-

pling pressure in determining m-line characteristics. For example, the waveguide could flow instead of bend under the coupling pressure. Thus, m-lines originating from polymer waveguides may well respond differently to the same coupling pressure applied to crystalline or glass waveguides.

Developing an experimental procedure to characterize the coupling gap for each measurement may not be simple. Even if we completely determine the coupling gap geometry, there are situations where we cannot use the previous models to recover the unperturbed effective index. For example, the analytical treatment in [4] applies only to cases of weak coupling, uniform gap, and infinite coupling length. The numerical techniques remove one of these limitations and allow cases of strong coupling. We attempt to address these limitations by introducing a numerical model of prism coupling based upon a local normal mode (LNM) expansion. Preliminary results from our model agree qualitatively with the first-order model of Section II. Figure 18 shows the m-line's irradiance profile with $x_r = 450 \mu\text{m}$ calculated using the LNM-model. This calculation uses a gap height $S = 0$ and infinite coupling length. Notice the exponential decay of the m-line's profile in Figure 18, which is also predicted by the first-order model.

We hope the results presented in this paper provide additional insights into effective index measurements using the prism coupler. Furthermore, these results indicate that to accurately measure effective index beyond the fourth decimal place using prism coupling will require additional experimental methods and theoretical models.

VII. ACKNOWLEDGMENTS

We acknowledge the support of the National Science Foundation under grant number ECS-9015752, the United States Army Research Office under grant number DAAL-03-92-G-0289 and the Office of Naval Research under grant number DOD ONR 14-92-J-1190. We also acknowledge assistance from Jeff Margolies with the acquisition of data set 1. Finally, we acknowledge many helpful editorial comments from Dr. Matt Young.

TABLES

TABLE I. Index of refraction for congruent lithium niobate [28] and rutile [29] at $\lambda = 0.6328 \mu\text{m}$ and $\lambda = 0.829 \mu\text{m}$.

	Lithium Niobate		Rutile	
Wave-length [μm]	Extra-ordinary Index of Refraction	Ordinary Index of Refraction	Extra-ordinary Index of Refraction	Ordinary Index of Refraction
$\lambda=0.6328$	2.2028	2.2865	2.8666	2.5821
$\lambda=0.829$	2.1728	2.2517	2.7789	2.5142

TABLE II. Set 1. Effective index versus coupling pressure for waveguide specimen 56 at $\lambda = 0.6328 \mu\text{m}$. The relationship between the coupling pressures is $P_1^{(1)} < P_2^{(1)}$.

Mode #	Low Coupling Pressure P_1	High Coupling Pressure P_2
TE 0	$2.2186 \pm 1.4 \times 10^{-4}$	$2.2164 \pm 1.4 \times 10^{-4}$
TE 3	$2.2039 \pm 1.8 \times 10^{-4}$	$2.2044 \pm 1.3 \times 10^{-4}$

TABLE III. Set 2. Effective index versus coupling pressure for waveguide specimen 56 at

$\lambda = 0.6328 \mu\text{m}$. The relationship between the pressures is $P_1^{(2)} < P_2^{(2)} < P_6^{(2)}$.

Mode #	Low Coupling Pressure P_1	Intermediate Coupling Pressure P_2 ($P_1 < P_2 < P_6$)	High Coupling Pressure P_6
TE 0	2.2168 ± 0.0002	2.2167 ± 0.0002	2.2165 ± 0.0002
TE 1	2.2063 ± 0.0002	2.2066 ± 0.0002	2.2065 ± 0.0002
TE 2	2.2045 ± 0.0002	2.2053 ± 0.0002	2.2048 ± 0.0002
TE 3	2.2034 ± 0.0002	2.2038 ± 0.0002	2.2036 ± 0.0002
TE 4		2.2034 ± 0.0002	2.2031 ± 0.0002

FIGURES

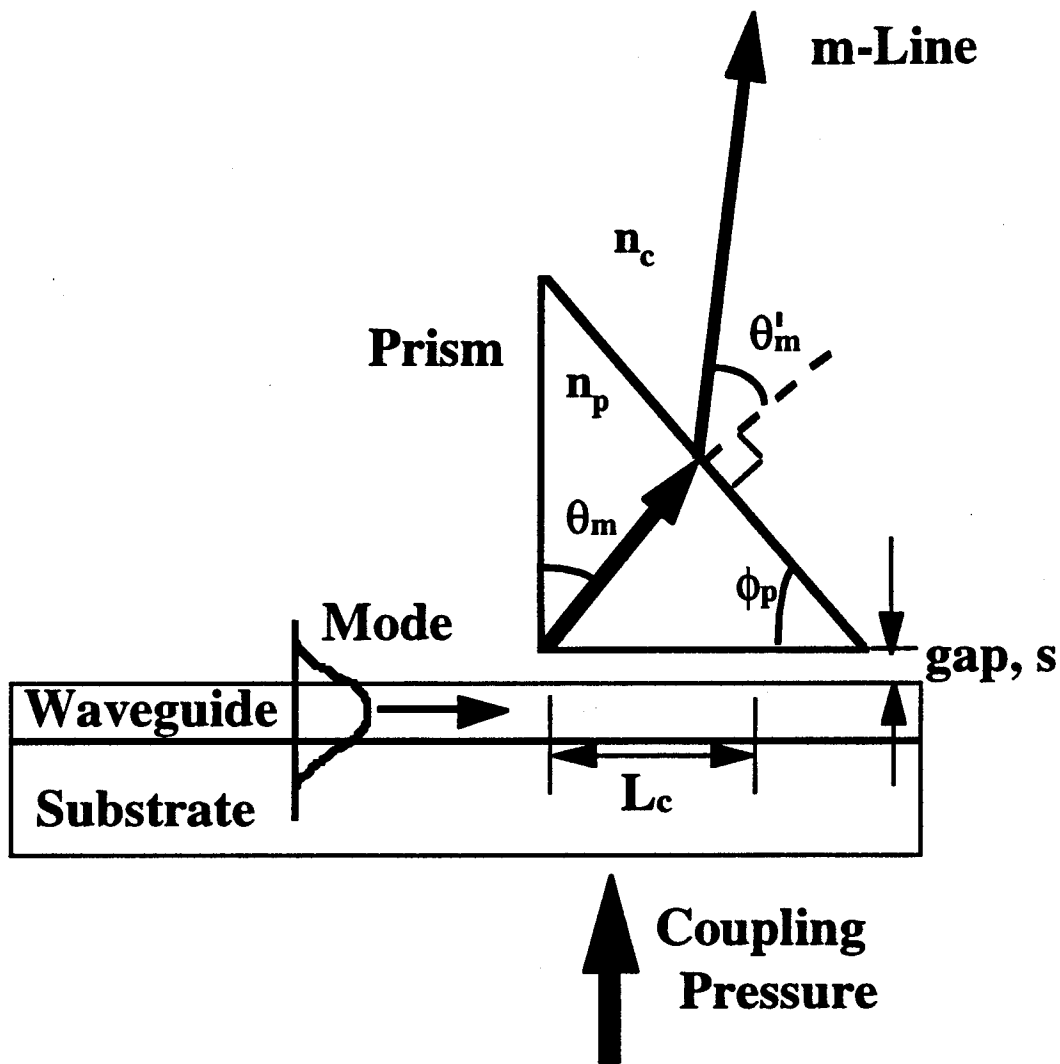


FIG. 1. Relevant features of the output prism-coupler. Effective index measurements reported in this paper were made using this prism-coupling arrangement.

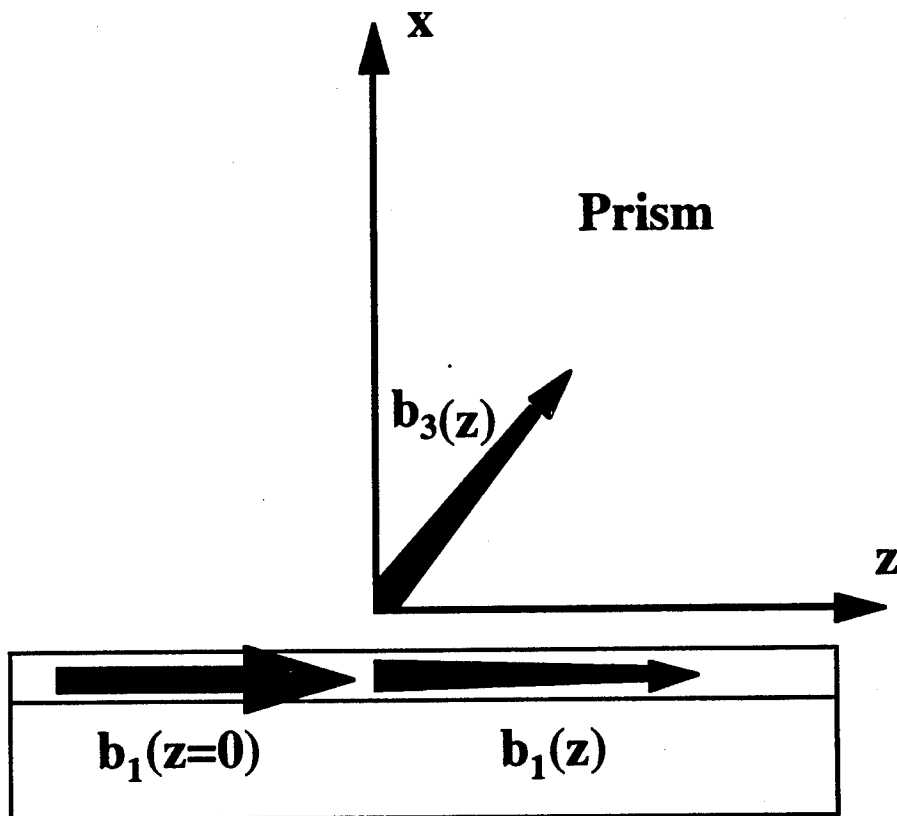


FIG. 2. Relationship between field amplitudes in Tien's [6] model describing output prism-coupling. The waveguide mode's initial field amplitude is $b_1(0)$. This field couples with the m-line field amplitude b_3 .

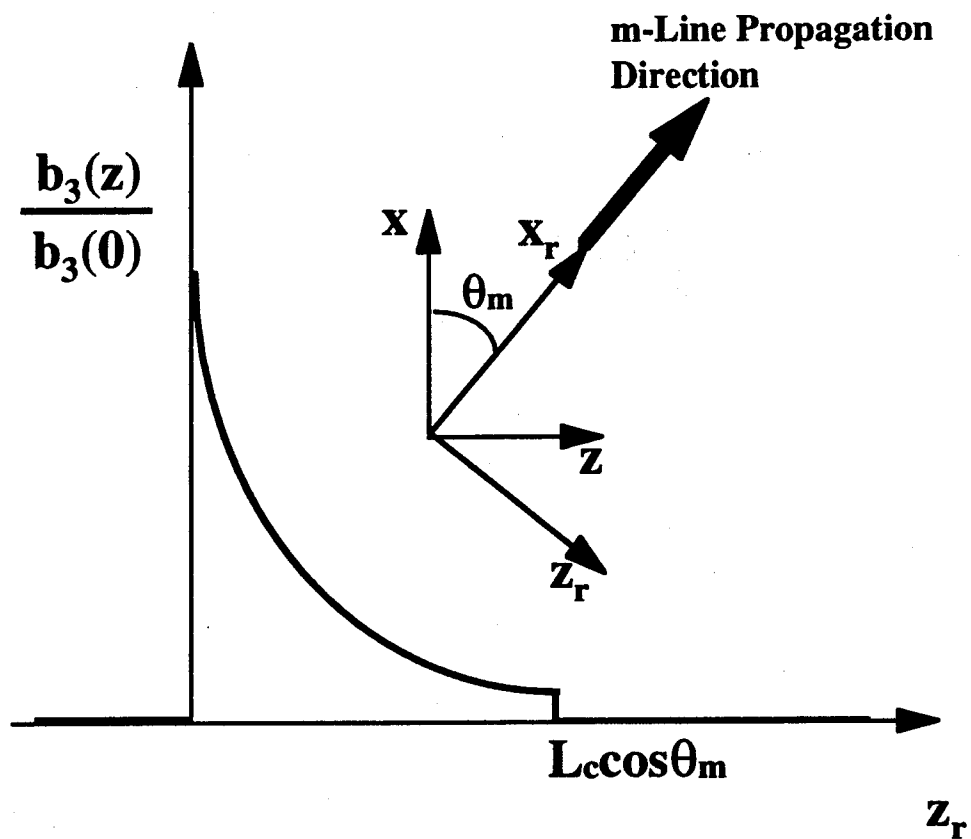


FIG. 3. Sketch of b_3 in the rotated coordinate system (x_r, z_r) . Also shown is the field truncation resulting from finite coupling length L_c .

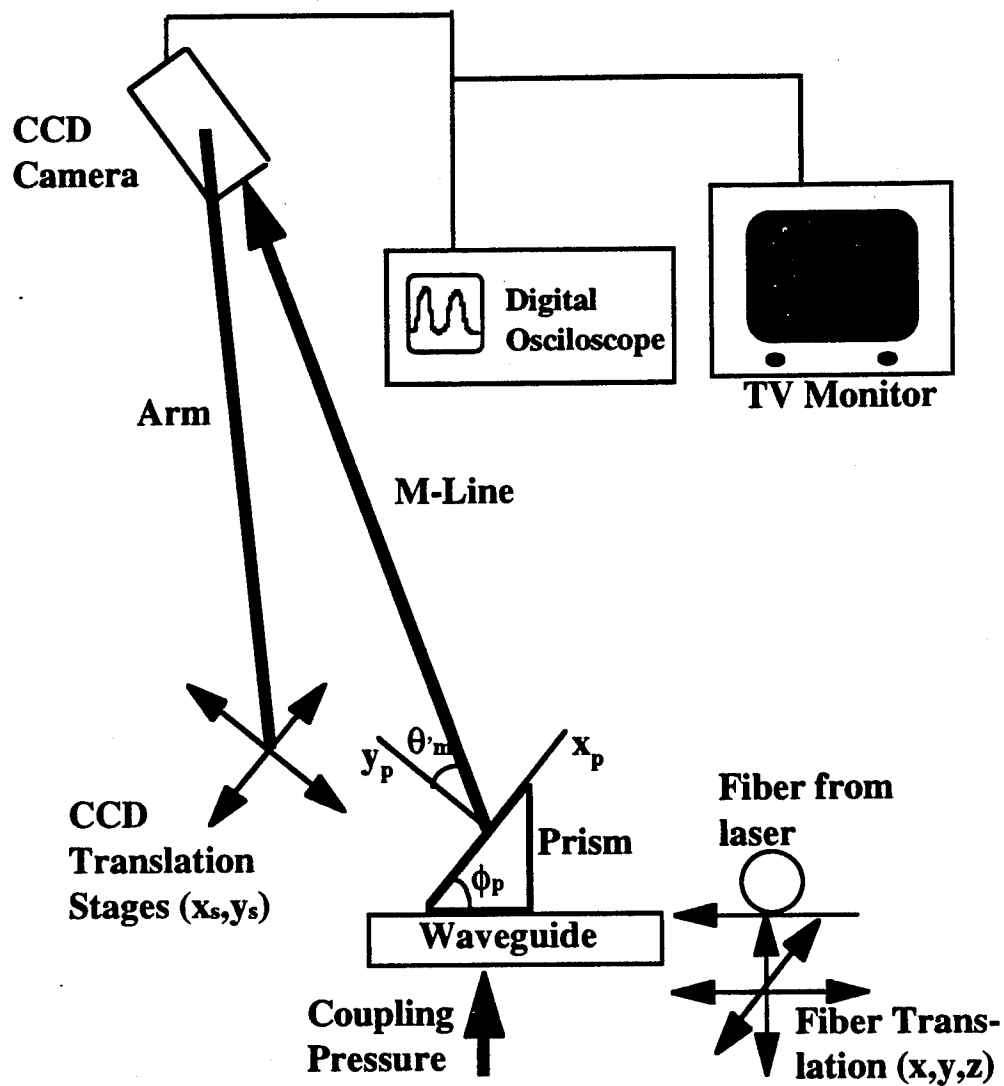


FIG. 4. Experimental setup for effective index measurements using output prism coupling.

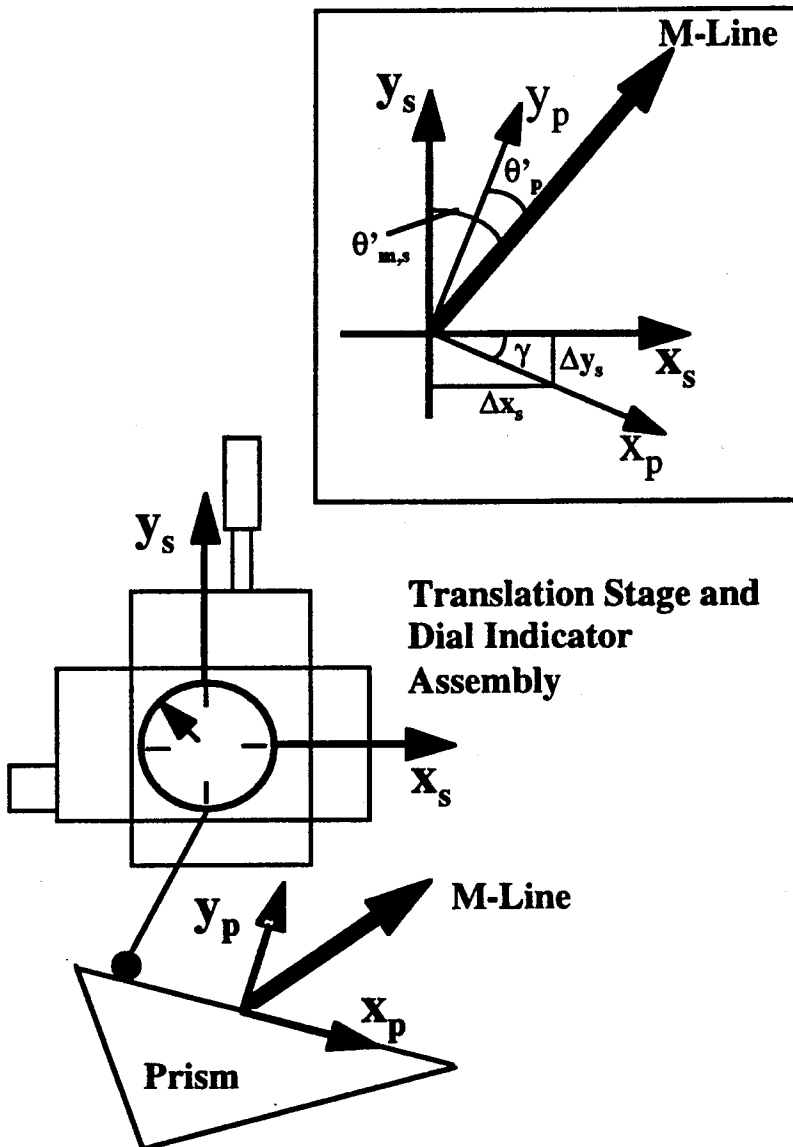


FIG. 5. Measuring the misalignment between the translation stages and the prism output face. Inset shows the relationship between the stage's coordinate system (x_s, y_s) and the prism's coordinate system (x_p, y_p) . The rotation angle between these two coordinate systems is γ .

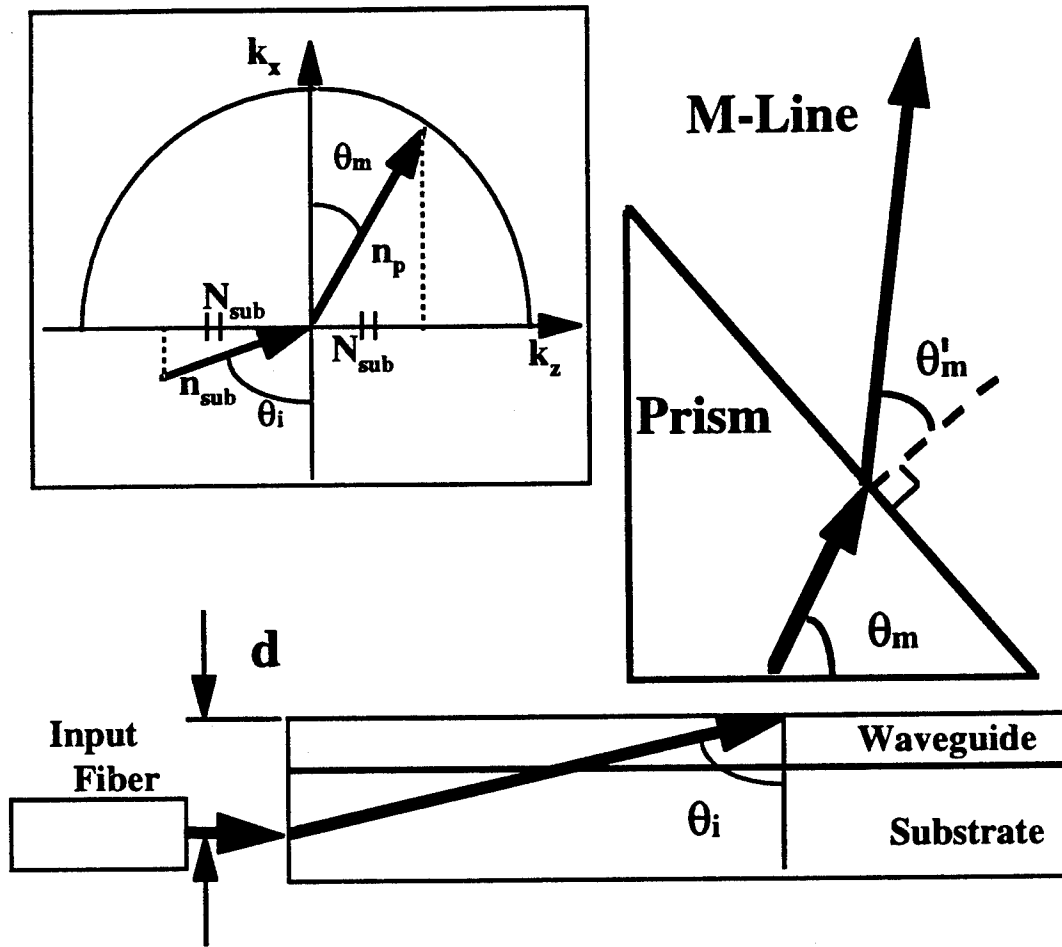


FIG. 6. Exciting the substrate radiation mode by positioning the input fiber. Inset illustrates the phase-matching condition Equation (1) for the substrate radiation mode. We use the substrate effective index for N_{sub} to reduce systematic uncertainties when measuring mode effective index.

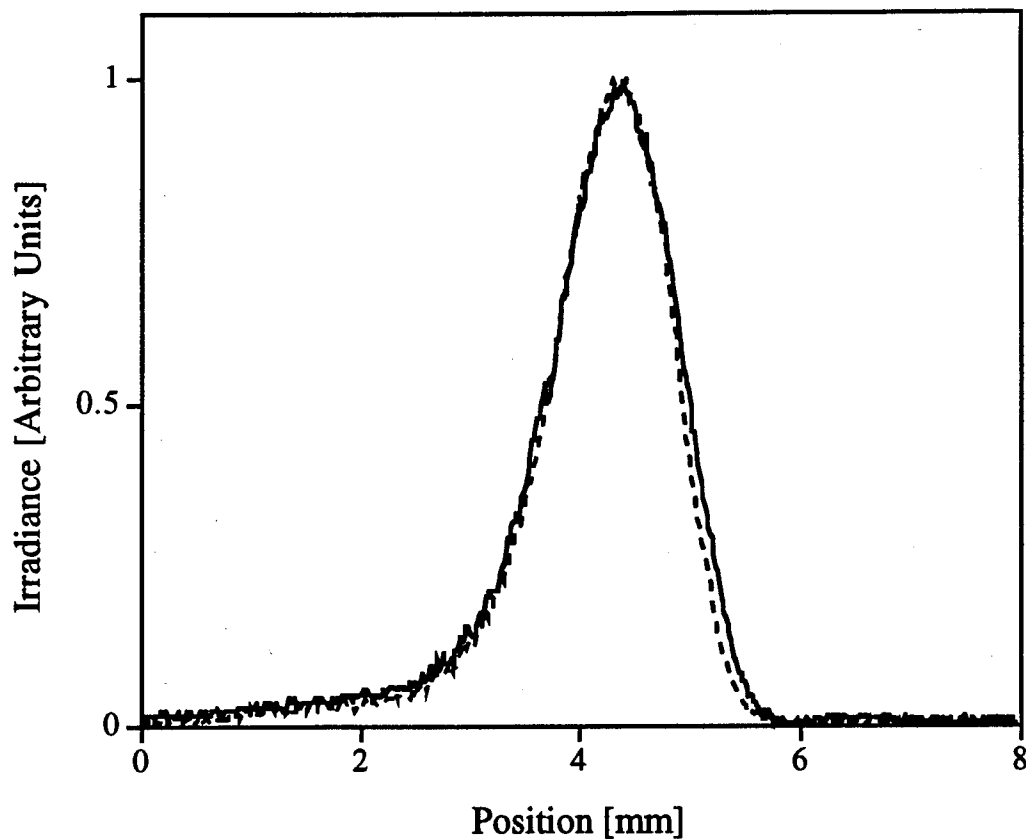


FIG. 7. Mode TE-0 m-line irradiance profiles of a titanium in-diffused slab waveguide ($\lambda = 0.6328 \mu\text{m}$) versus position along the CCD array. The solid curve corresponds to the far propagation distance while the dashed curve corresponds to the near propagation distance. The difference between propagation distances is 50.00 mm. These irradiance profiles have been normalized to 1 and shifted so that their maximum values coincide.

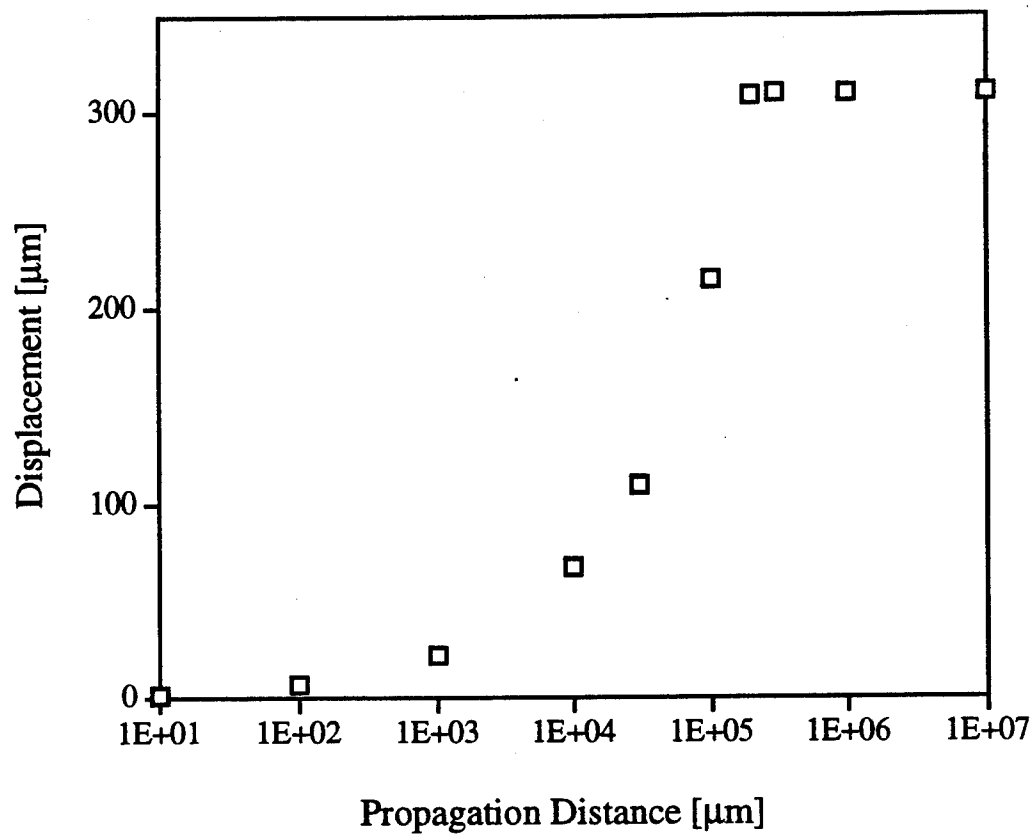


FIG. 8. Displacement of m-line maximum irradiance from far-field propagation direction versus propagation distance.

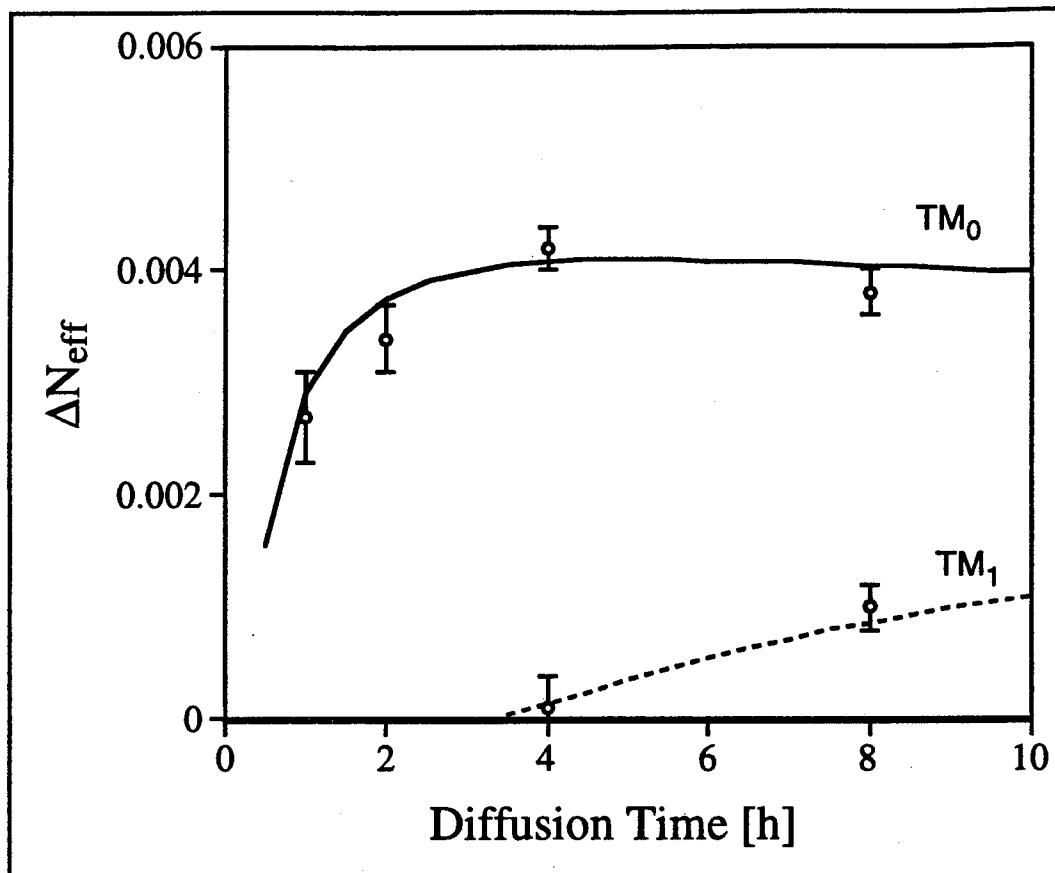


FIG. 9. Increment above the substrate index of refraction for mode effective index versus diffusion time. The fundamental mode's effective index is TM-0 and that of the first higher order mode is TM-1. Theoretical curves are fitted to measured data points using the parameters in Equation (23).

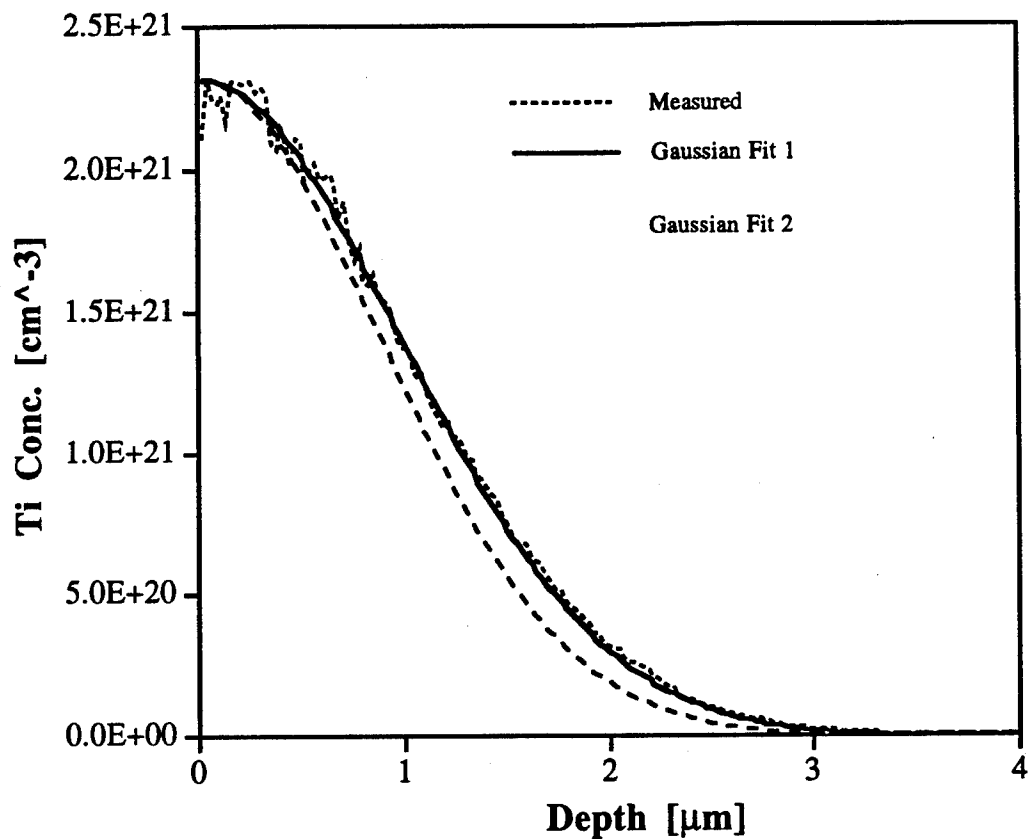


FIG. 10. Titanium concentration versus substrate depth for 2 h diffusion (specimen 42). SIMS data are the short-dash curve. The solid curve is a Gaussian fit using $D = 0.245 \mu\text{m}^2/\text{h}$. The long-dash curve is a Gaussian fit using $D = 0.2 \mu\text{m}^2/\text{h}$.

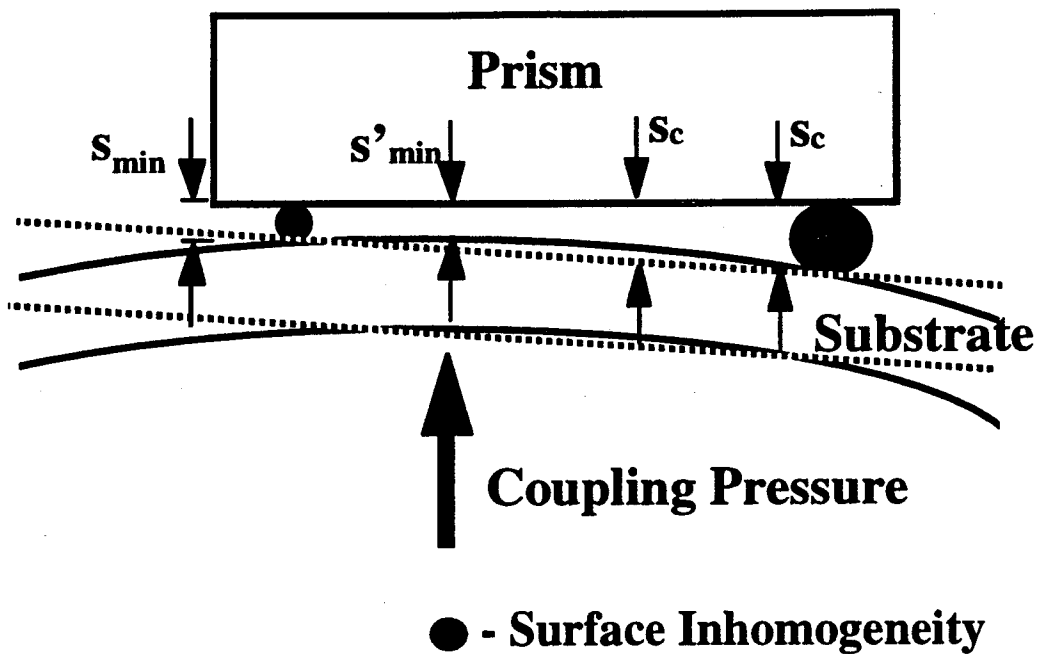


FIG. 11. Schematic cross section of prism coupling region. The substrate outlined by the dashed line is for the initial low coupling pressure. The substrate outlined by the solid line is for high coupling pressure.

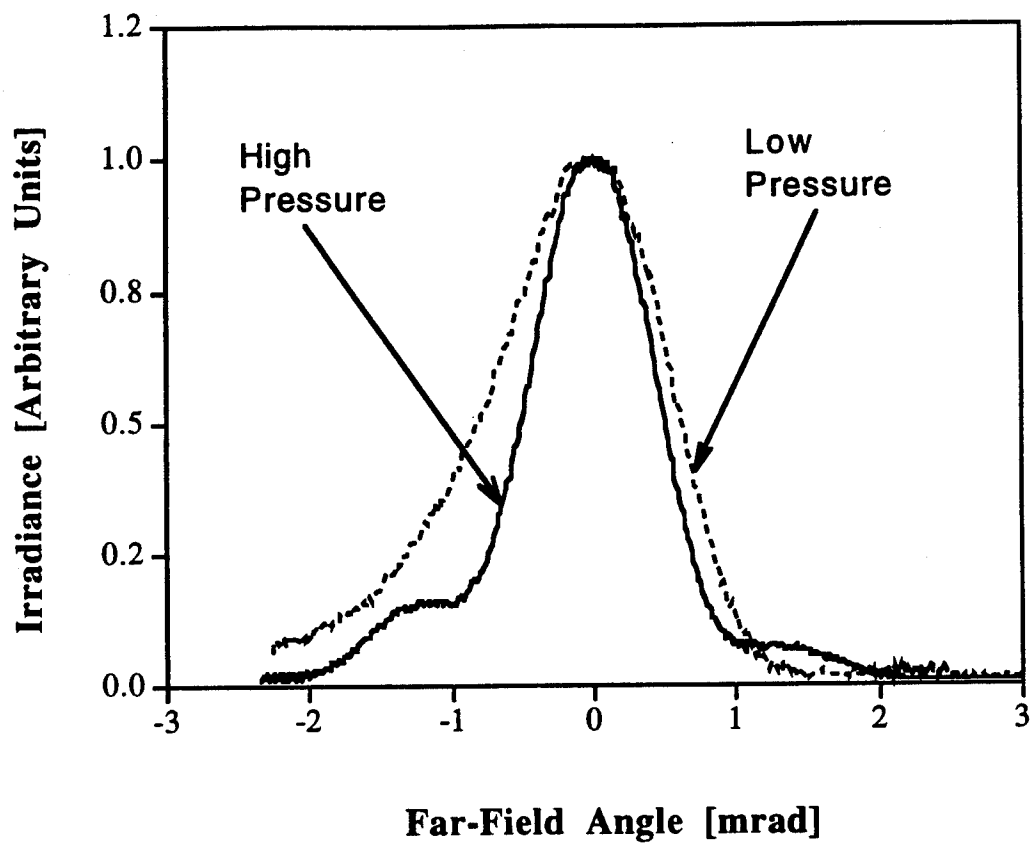


FIG. 12. Comparing Set 1 TE-0 m-line profiles for low $P_1^{(1)}$ and high $P_2^{(1)}$ coupling pressures.

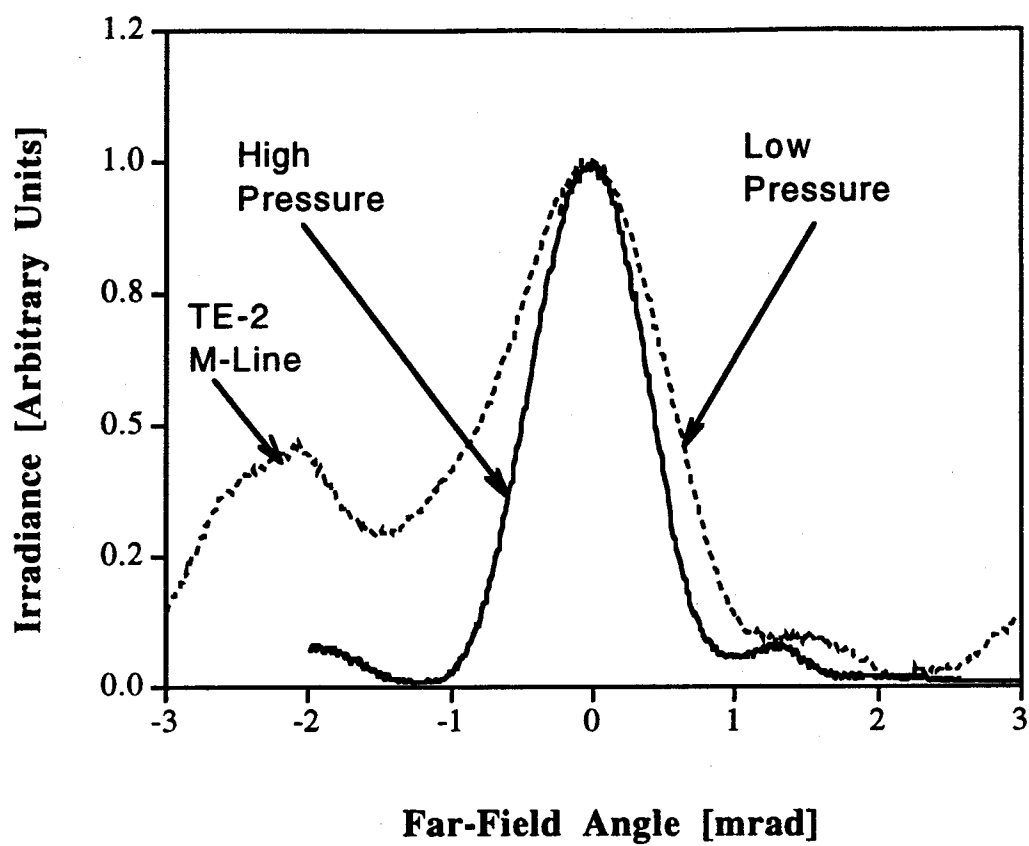


FIG. 13. Comparing Set 1 TE-3 m-line profiles for low $P_1^{(1)}$ and high $P_2^{(1)}$ coupling pressures.

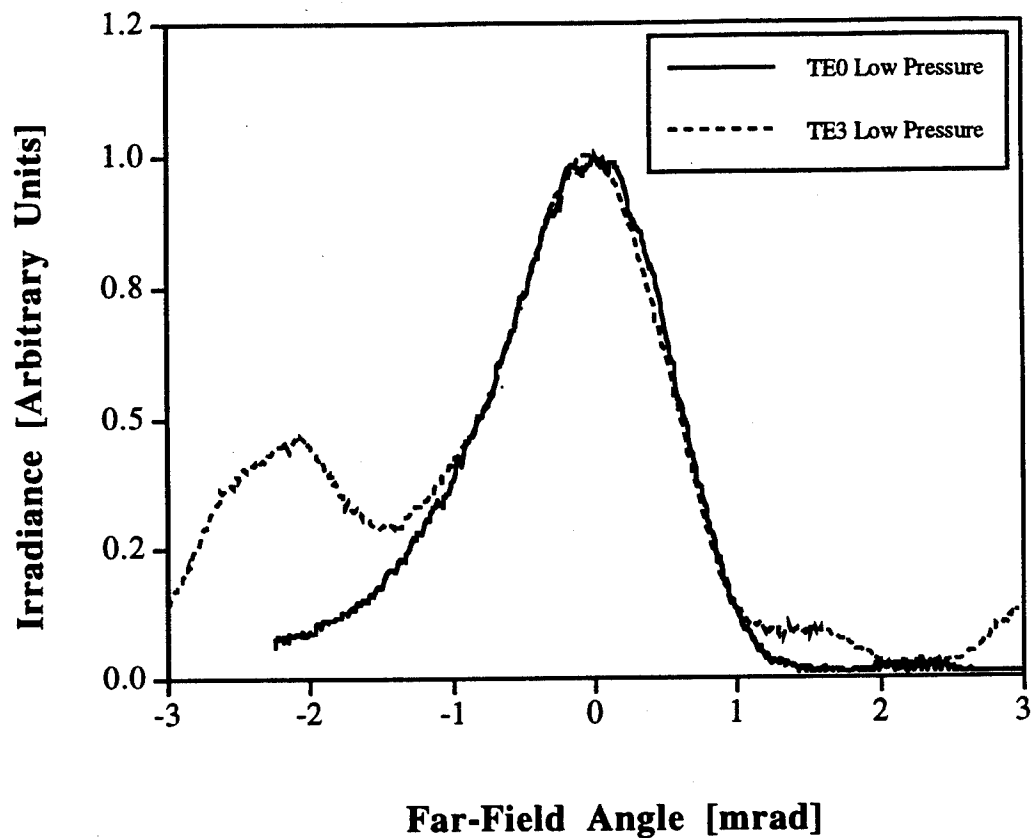


FIG. 14. Comparing Set 1 TE-0 m-line profile to the TE-3 m-line profile when the coupling pressure is low $P_1^{(1)}$.

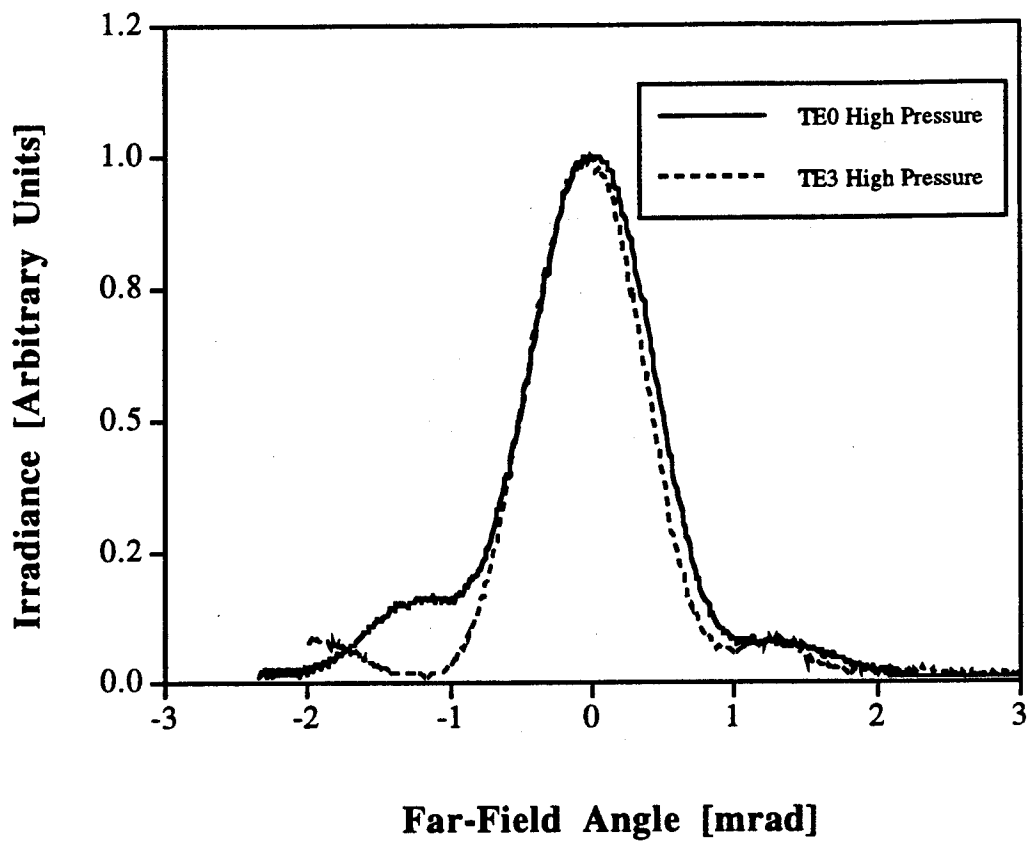


FIG. 15. Comparing Set 1 TE-0 m-line profile to the TE-3 m-line profile when the coupling pressure is high $P_2^{(1)}$.

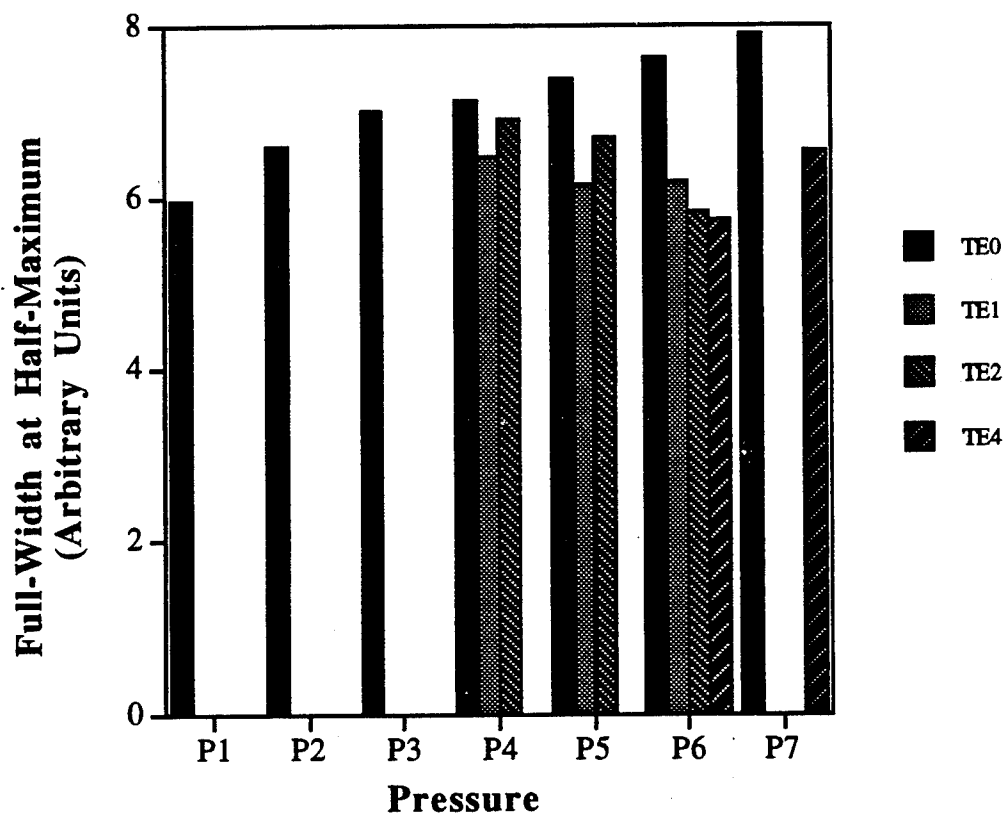


FIG. 16. Measurements of m-line's irradiance profile full-width at half-maximum at various coupling pressures of Set 2. The coupling pressures increases from $P_1^{(2)}$ to $P_7^{(2)}$.

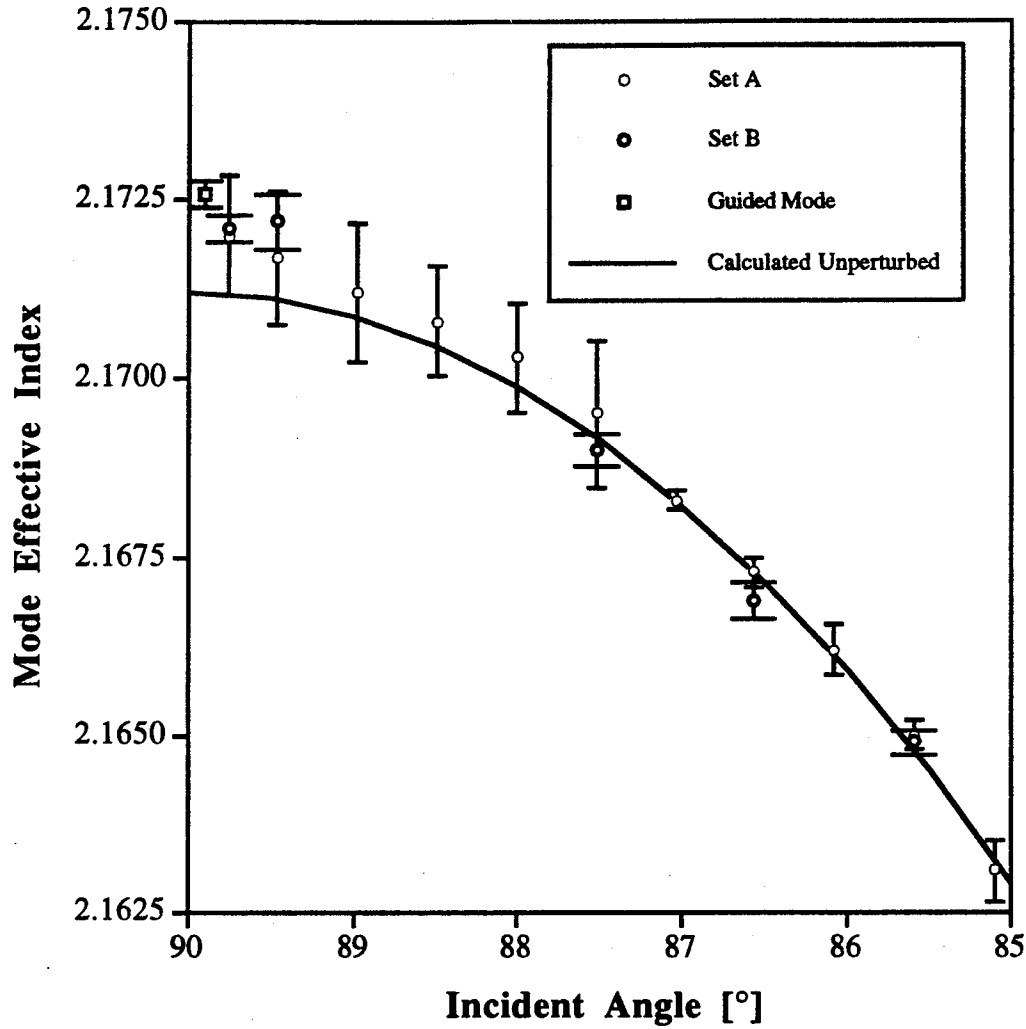


FIG. 17. Measuring the TE substrate mode effective index versus angle of incidence θ_i at $\lambda = 0.829 \mu\text{m}$. The open circles represent measurement set A while the filled circles represent measurement set B. The continuous line is a fit to the measured data for $\theta_i < 87.5^\circ$ using the first-order model which ignores the prism-waveguide perturbation. This fit yields an effective index of 2.1712 at $\theta_i = 90^\circ$. The filled square represents the highest order TE guided mode effective index. We have widened the uncertainty bars of data set B as a graphical visualization aid.

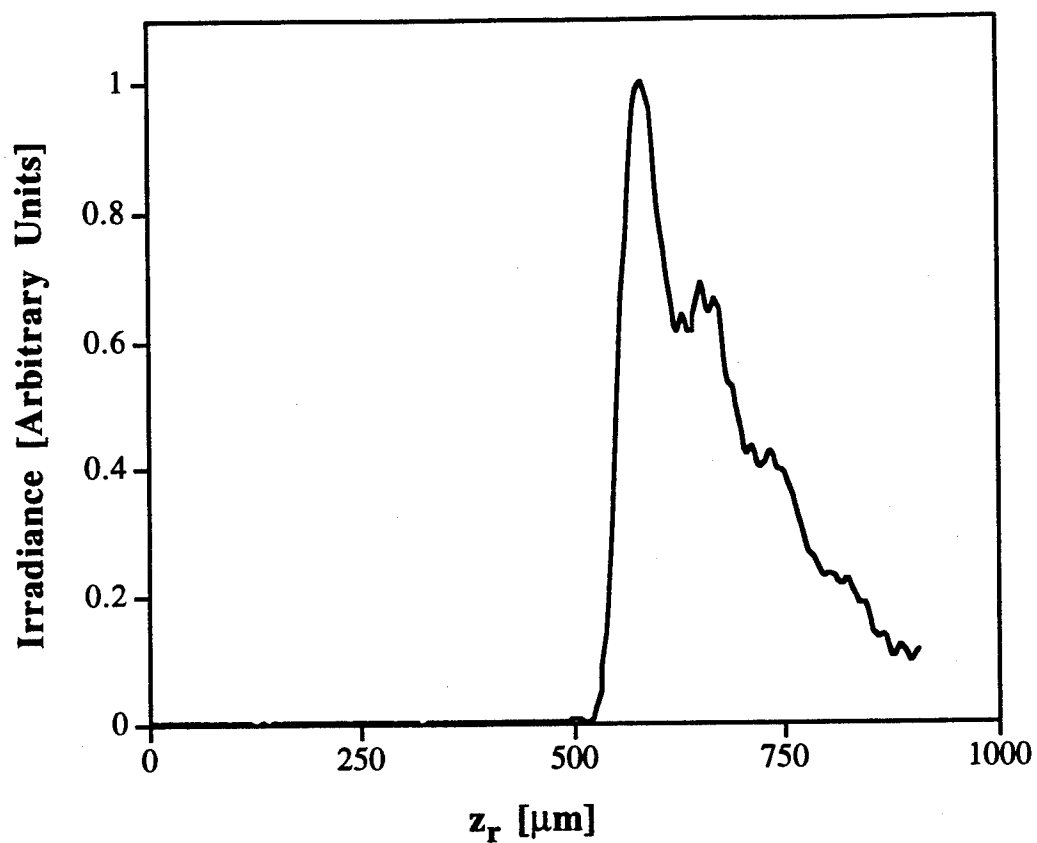


FIG. 18. M-line irradiance profile calculated using the local normal mode expansion of output prismcoupling.

REFERENCES

- [1] T. Tamir, *Integrated Optics*. Berlin, New York: Springer-Verlag, second ed., 1985.
- [2] H. Osterberg and L. W. Smith, "Transmission of optical energy along surfaces: Part ii, inhomogeneous media," *J. Opt. Soc. Am.*, vol. 54, pp. 1078-1084, 1964.
- [3] P. Tien and R. Ulrich, "Theory of prism-film coupler and thin-film light guides," *J. Opt. Soc. Amer.*, vol. 60, pp. 1325-1337, 1970.
- [4] R. Ulrich, "Theory of the prism-film coupler by plane-wave analysis," *J. Opt. Soc. Amer.*, vol. 60, pp. 1337-1350, 1970.
- [5] J. E. Midwinter, "Evanescent field coupling into a thin-film waveguide," *IEEE J. Quantum Electron.*, vol. 6, pp. 123-130, 1970.
- [6] P. K. Tien, "Light waves in thin films and integrated optics," *Appl. Opt.*, vol. 10, pp. 2395-2413, 1971.
- [7] R. Ulrich, "Optimum excitation of optical surface waves," *J. Opt. Soc. Amer.*, vol. 61, pp. 1467-1477, 1971.
- [8] T. Tamir and H. L. Bertoni, "Lateral displacement of optical beams at multilayered and periodic structures," *J. Opt. Soc. Amer.*, vol. 61, pp. 1397-1413, 1971.
- [9] R. T. Kersten, "The prism-film coupler as a precision instrument part i. accuracy and capabilities of prism couplers as instruments," *Optica Acta*, vol. 22, pp. 503-513, 1975.
- [10] J. S. Wei and W. D. Westwood, "A new method for determining thin-film refractive index and thickness using guided optical waves," *Appl. Phys. Lett.*, vol. 32, pp. 819-821, 1978.
- [11] H. J. W. M. Hoekstra, J. C. van't Spijker, and H. M. M. K. Koerkamp, "Ray picture for prism-film coupling," *J. Opt. Soc. Am. A.*, vol. 10, pp. 2226-2230, 1993.

- [12] J. D. Swalen, M. Tacke, R. Santo, K. E. Rieckhoff, and K. Fischer, "Spectra of organic molecules in thin films," *Helvetica Chimica Acta*, vol. 61, pp. 960-977, 1978.
- [13] J. Chilwell and I. Hodgkinson, "Thin-films field-transfer matrix theory of planar multilayer waveguides and reflection from prism-loaded waveguides," *J. Opt. Soc. Am. A*, vol. 1, pp. 742-753, 1984.
- [14] L. M. Walpita, "Solutions for planar optical waveguide equations by selecting zero elements in a characteristic matrix," *J. Opt. Soc. Am. A*, vol. 2, pp. 595-602, 1985.
- [15] A. K. Ghatak, K. Thyagarajan, and M. R. Shenoy, "Numerical analysis of planar optical waveguides using matrix approach," *J. Lightwave Technol.*, vol. 5, pp. 660-667, 1987.
- [16] P. K. Tien, R. Ulrich, and R. J. Martin, "Modes of propagating light waves in thin deposited semiconductor films," *Appl. Phys. Lett.*, vol. 14, pp. 291-294, 1969.
- [17] R. Ulrich and R. Torge, "Measurement of thin film parameters with a prism coupler," *Appl. Opt.*, vol. 12, pp. 2901-2908, 1973.
- [18] R. T. Kersten, "The prism-file coupler as a precision instrument part ii. measurements of refractive index and thickness of leaky waveguides," *Optica Acta*, vol. 22, pp. 515-521, 1975.
- [19] S. Morasca and C. De Bernardi, "High accuracy determination of semiconductor substrate and waveguide refractive index by prism coupling," in *Integrated Optical Circuit Engineering VI*, Vol. 993, SPIE, 1988, pp. 164-166.
- [20] D. Marcuse, *Theory of Dielectric Optical Waveguides*. New York: Academic Press, first ed., 1974.
- [21] A. R. Mickelson, *Guided Wave Optics*. New York: Van Nostrand Reinhold, first ed., 1992.
- [22] J. W. Goodman, *Introduction to Fourier Optics*. San Francisco: McGraw-Hill, first ed.,

1968.

- [23] R. V. Schmidt and I. P. Kaminow, "Metal-diffused optical waveguides in LiNbO₃ films," *Appl. Phys. Lett.*, vol. 25, pp. 458-460, 1974.
- [24] J. R. Carruthers, I. P. Kaminow, and L. W. Stulz, "Diffusion kinetics and optical waveguiding properties of out-diffused layers in lithium niobate and lithium tantalate," *Appl. Opt.*, vol. 13, pp. 2333-2342, 1974.
- [25] S. L. Kwiatkowski and A. R. Mickelson, "Nearly cut-off modes caused by diffusion in lithium niobate," *J. Appl. Phys.*, vol. 76, pp. 5877-5885, 1994.
- [26] J. Crank, *The Mathematics of Diffusion*. New York: Oxford University Press, second ed., 1986.
- [27] J. Vollmer, J. P. Nisius, P. Hertel, and E. Krätzig, "Refractive index profiles of LiNbO₃:Ti waveguides," *Appl. Phys. A*, vol. 32, pp. 125-127, 1983.
- [28] D. F. Nelson and R. M. Mikulyak, "Refractive indices of congruently melting lithium niobate," *J. Appl. Phys.*, vol. 45, pp. 3688-3689, 1974.
- [29] W. L. Bond, "Measurement of the refractive indices of several crystals," *J. Appl. Phys.*, vol. 36, pp. 1674-1677, 1965.

List of Tables

I	Index of refraction for congruent lithium niobate [28] and rutile [29] at $\lambda = 0.6328 \mu\text{m}$ and $\lambda = 0.829 \mu\text{m}$	24
II	Set 1. Effective index versus coupling pressure for waveguide specimen 56 at $\lambda = 0.6328 \mu\text{m}$. The relationship between the coupling pressures is $P_1^{(1)} < P_2^{(1)}$	25
III	Set 2. Effective index versus coupling pressure for waveguide specimen 56 at $\lambda = 0.6328 \mu\text{m}$. The relationship between the pressures is $P_1^{(2)} < P_2^{(2)} < P_6^{(2)}$	26

List of Figures

1	Relevant features of the output prism-coupler. Effective index measurements reported in this paper were made using this prism-coupling arrangement. . .	27
2	Relationship between field amplitudes in Tien's [6] model describing output prism-coupling. The waveguide mode's initial field amplitude is $b_1(0)$. This field couples with the m-line field amplitude b_3	28
3	Sketch of b_3 in the rotated coordinate system (x_r, z_r) . Also shown is the field truncation resulting from finite coupling length L_c	29
4	Experimental setup for effective index measurements using output prism coupling.	30
5	Measuring the misalignment between the translation stages and the prism output face. Inset shows the relationship between the stage's coordinate system (x_s, y_s) and the prism's coordinate system (x_p, y_p) . The rotation angle between these two coordinate systems is γ	31
6	Exciting the substrate radiation mode by positioning the input fiber. Inset illustrates the phase-matching condition Equation (1) for the substrate radiation mode. We use the substrate effective index for N_{sub} to reduce systematic uncertainties when measuring mode effective index.	32
7	Mode TE-0 m-line irradiance profiles of a titanium in-diffused slab waveguide ($\lambda = 0.6328 \mu\text{m}$) versus position along the CCD array. The solid curve corresponds to the far propagation distance while the dashed curve corresponds to the near propagation distance. The difference between propagation distances is 50.00 mm. These irradiance profiles have been normalized to 1 and shifted so that their maximum values coincide.	33
8	Displacement of m-line maximum irradiance from far-field propagation direction versus propagation distance.	34

9	Increment above the substrate index of refraction for mode effective index versus diffusion time. The fundamental mode's effective index is TM-0 and that of the first higher order mode is TM-1. Theoretical curves are fitted to measured data points using the parameters in Equation (23).	35
10	Titanium concentration versus substrate depth for 2 h diffusion (specimen 42). SIMS data are the short-dash curve. The solid curve is a Gaussian fit using $D = 0.245 \mu\text{m}^2/\text{h}$. The long-dash curve is a Gaussian fit using $D = 0.2 \mu\text{m}^2/\text{h}$	36
11	Schematic cross section of prism coupling region. The substrate outlined by the dashed line is for the initial low coupling pressure. The substrate outlined by the solid line is for high coupling pressure.	37
12	Comparing Set 1 TE-0 m-line profiles for low $P_1^{(1)}$ and high $P_2^{(1)}$ coupling pressures.	38
13	Comparing Set 1 TE-3 m-line profiles for low $P_1^{(1)}$ and high $P_2^{(1)}$ coupling pressures.	39
14	Comparing Set 1 TE-0 m-line profile to the TE-3 m-line profile when the coupling pressure is low $P_1^{(1)}$	40
15	Comparing Set 1 TE-0 m-line profile to the TE-3 m-line profile when the coupling pressure is high $P_2^{(1)}$	41
16	Measurements of m-line's irradiance profile full-width at half-maximum at various coupling pressures of Set 2. The coupling pressures increases from $P_1^{(2)}$ to $P_7^{(2)}$	42

- 17 Measuring the TE substrate mode effective index versus angle of incidence θ_i at $\lambda = 0.829 \mu\text{m}$. The open circles represent measurement set A while the filled circles represent measurement set B. The continuous line is a fit to the measured data for $\theta_i < 87.5^\circ$ using the first-order model which ignores the prism-waveguide perturbation. This fit yields an effective index of 2.1712 at $\theta_i = 90^\circ$. The filled square represents the highest order TE guided mode effective index. We have widened the uncertainty bars of data set B as a graphical visualization aid. 43
- 18 M-line irradiance profile calculated using the local normal mode expansion of output prismcoupling. 44